SM Compatibility of $B \to K^{(*)}\pi$ Measurements and Analysis on $B^+ \to K^*(892)^+\pi^0$ in Belle II

Kompatibilität der $B \to K^{(*)}\pi$ Messungen und Analyse des Kanals $B^+ \to K^*(892)^+\pi^0$ in Belle II

Masterarbeit aus der Physik

Vorgelegt von
Oskar Tittel
March 14, 2021

Fakultät für Physik
Ludwig-Maximilians-Universität München
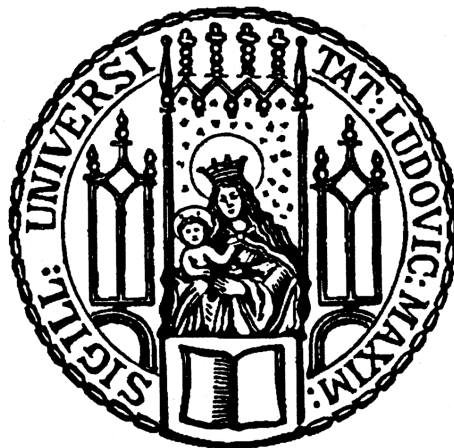
Betreuer: Prof. Dr. Christian Kiesling

Abstract

In 2001, the BaBar and Belle experiments have convincingly confirmed the CP violation within the B meson system as predicted by the Standard Model (SM). However, "tensions" have been observed between particular measurements and the corresponding SM prediction. To investigate these tensions and potentially find physics beyond the SM, the Belle experiment has been upgraded to Belle II. Here, a massive luminosity upgrade has been realized for the KEK B factory (KEKB) collider in Tsukuba, Japan. The new Super KEK B factory (SuperKEKB) accelerator aims for an instantaneous luminosity of $\mathcal{L} = 6 \times 10^{35} \mathrm{cm}^{-2}\,\mathrm{s}^{-1}$, which is 30 times the record of its predecessor. Together with the improved Belle II detector, this experiment will enable high precision tests on the SMin the near future. As a first look into the potential of the new detector, measurements on B physics are now performed. Interesting channels are $B \to K^{(*)}\pi$, where tree diagrams are suppressed, enhancing the sensitivity to loop diagrams, which are sensitive to New Physics (NP).

In anticipation of these more precise results, the current status of the theoretical implications from the $B \to K\pi$ are evaluated. It is shown, that a fit which only includes the leading order diagrams fails to explain the experimental results. This is called the $K\pi$-puzzle. With the introduction of the color suppressed tree diagram with a naive color suppression factor compared to the color allowed tree process, the tensions of the $K\pi$-puzzle can be resolved within the SM and the data can be fit with a quality of $\frac{\chi^2}{d.o.f.} = 5.6/4$. However, including a constraint from the measurement on the branching ratio (BR) of $B \to \pi^+\pi^0$ creates further tensions. These tensions can be partly resolved by letting the color suppressed tree amplitude float freely, which results in a fit quality of $\frac{\chi^2}{d.o.f.} = 7.7/4$. $B^0 \to K^0\pi^0$ has been identified as a key measurement in Belle II to either resolve these tensions or increase their significance. In the $B \to K^*\pi$ system, neither the leading amplitudes approximation nor the introduction of a free color suppressed diagram could fit the diagrams with reasonable quality. The best fit only includes the leading orders and achieved a result of $\frac{\chi^2}{d.o.f.} = 12.2/3$. The large measurement errors hinder a more sophisticated analysis. Thus, more precise measurements are needed to constrain the parameter space for these decays. Here, $A_{CP}(B \to K^{*0}\pi^0)$ has been identified a key measurement for Belle II.

In the last part of the thesis, the current analysis on the decay $B^+ \to K^*(892)^+[K_S^0\pi^+]\pi^0$ is presented. The event reconstruction and optimization cut for the background suppression are discussed. Then, a working 2D fit on the decay in ΔE and M_{bc} is presented. The fit successfully models the signal, but still fails to distinguish continuum and $B\bar{B}$ background. In addition, a working A_{CP} fit is in place. In the time frame of this thesis, the analysis could not be completed. Next steps are a candidate selection and the investigation of systematic uncertainties.

Contents

1 Introduction

Following Sakharov [1], three basic requirements have to be met for the emergence of a matter dominated universe. These, so-called Sakharov conditions are the violation of the baryon number, thermal disequilibrium in the early universe and a violated matter-antimatter symmetry. The last condition includes the violation of the charge (C) and charge-parity (CP) conjugation. The CP violation was introduced into the Standard Model (SM) with the Cabibbo-Kobayashi-Maskawa (CKM) mechanism [2]. In 2001, two independent experiments, the BaBar experiment in the USA and the Belle experiment in Japan, could verify the existence of CP violation in the B meson system, in agreement with the SM predictions [3] [4]. Following this discovery, Kobayashi and Maskawa won the Nobel Prize in physics in 2008. Although CP violation has been observed, the measured strength is orders of magnitude too small to explain the difference between matter and antimatter in the universe. Next to the presence of dark matter and dark energy in the universe, this is one of the big unsolved mysteries in particle and astrophysics.

In order to enhance our physical understanding of the world and find NP beyond the SM, two approaches have been chosen in particle physics. The first one is to increase the collision energies of accelerators in order to directly produce heavy particles, which have not been observed before. This path is pursued by the Large Hadron Collider (LHC) at the Conseil Européen pour la Recherche Nucléaire (CERN). The LHC operates at a center-of-mass energy of 14TeV in proton collisions. The second approach is the high precision approach. Here, the aim is to increase the number of recorded collisions as far as possible. This enables more precise measurements, which could show the impact of high mass NP particles as virtual particles in loops.

This strategy is pursued by the upgrade of the Belle experiment, Belle II. The corresponding SuperKEKB accelerator, which is located in Tsukukba, Japan, aims for an instantaneous luminosity of $\mathcal{L} = 6 \times 10^{35} \mathrm{cm}^{-2}\,\mathrm{s}^{-1}$. This corresponds to 30 times the old world record of KEKB. The accelerator collides electrons and positrons with different energies at total center-of-mass energies around 10.58GeV, which is the resonance of the $\Upsilon(4S)$. The $\Upsilon(4S)$ primarily decays into a system of two B mesons. The investigations of B meson decays with the increased luminosity at Belle II will produce the most precise measurements on B physics and significant checks of the SM. In this regard, measurements on $B \to K\pi$ decays will be of special interest, since the measured asymmetries have shown some tensions known as the $K\pi$-puzzle. The set of $B \to K\pi$ and $B \to K^*\pi$ decays will

be the subject of this thesis.

Chapter 2 first covers the SM of particle physics. This includes a brief discussion of the different kinds of particles and the fundamental forces covered by the SM. Then, the concept of symmetries is introduced, the parity (P), charge (C), and time (T) conjugation are presented and their violations are discussed. Finally, the CKM formalism is introduced, leading to its consequences for B physics and a short discussion of the B meson production mechanism and flavor tagging.

Chapter 3 discusses the SuperKEKB collider, mainly focusing on the luminosity of the accelerator. In addition, the Belle II detector is presented. This includes a short introduction of all sub-detectors and their purpose.

Chapter 4 covers the current state of the measurements on $B \to K^{(*)}\pi$ decays. An introduction to the SM expectations for the decays and the theoretical calculations for the branching ratios (BRs) and asymmetries leads to the presentation of a fitting method. Using this method, the measurements on the $B \to K^{(*)}\pi$ are fitted using different approximations. For the $B \to K\pi$ system, a possible solution for the $K\pi$-puzzle within the SM is discussed. Then, important measurements for Belle II are identified in the system also involving an additional constraint from the decay $B \to \pi^+\pi^0$.

Chapter 5 displays the current state of the Belle II analysis on the decay $B^+ \to K^*(892)^+[K_S^0\pi^+]\pi^0$. First, an outline of the event reconstruction this given, which is followed by the suppression of the continuum background and the optimization of the signal selection. Then, the current BR fits and the obtained direct CP violation from simulated data are shown. Lastly, further possible steps in the analysis are discussed.

Chapter 6 reviews and concludes the results from the presented studies. In addition, further steps are discussed and an outlook towards future developments is given.

2 Theory

2.1 The Standard Model

The Standard Model (SM) is a quantum theory describing the elementary particles and their interactions. Elementary particles have no substructure, meaning that they are the fundamental building blocks of all matter. The interactions covered by the SM are the strong, the electromagnetic and the weak force, which follow the order of strength in which they have been named. Gravity as the last and weakest fundamental force is not included in the SM. For particle processes this is not a problem, since gravity is so weak that it can be neglected here. Furthermore, there is no viable theoretical concept at present to formulate gravity as a relativistic quantum theory. In the SM, the forces are mediated via exchange bosons. All particles in the SM including the exchange particles are displayed in figure 2.1. The given charges in this picture and the following explanations are in units of the elementary charge e.

The SM particles can be divided into two subgroups. First, the fermions, the building blocks of matter (which are displayed in purple and green) have a half-integer spin. The bosons, mediating the forces between the fermions (red and yellow) on the other hand have an integer spin.

Leptons are a subgroup of the fermions, which are grouped in three generations. Each generation consists of a negatively charged particle (electron, muon, tauon) and corresponding neutrino, which has no charge. While the masses of the electron, the muon and the tauon are well measured and increase with the generations, the masses of the neutrinos are neglected in the SM but known to be non-zero. All leptons carry a lepton number, specific for the generation. The leptons displayed here carry the number $+1$ while their anti-particle carry the lepton number -1. The lepton numbers are individually conserved quantum numbers.

The second subgroup of the fermions, the quarks, are separated in three different generations. Each generation consists of one up-type quark with a charge of $+\frac{2}{3}$ and one down-type quark with charge $-\frac{1}{3}$. The up-type quarks are the up, charm and top quark (u, c, t) and the corresponding down-type quarks are the down, strange and bottom quark (d, s, b) respectively. The masses of the quarks rise with the generations, and similarly to the leptons, they carry a quantum number, the weak isospin. The weak isospin (I_z) of up-type quarks and anti-down-type quarks is $+\frac{1}{2}$, while the isospin of

Standard Model of Elementary Particles
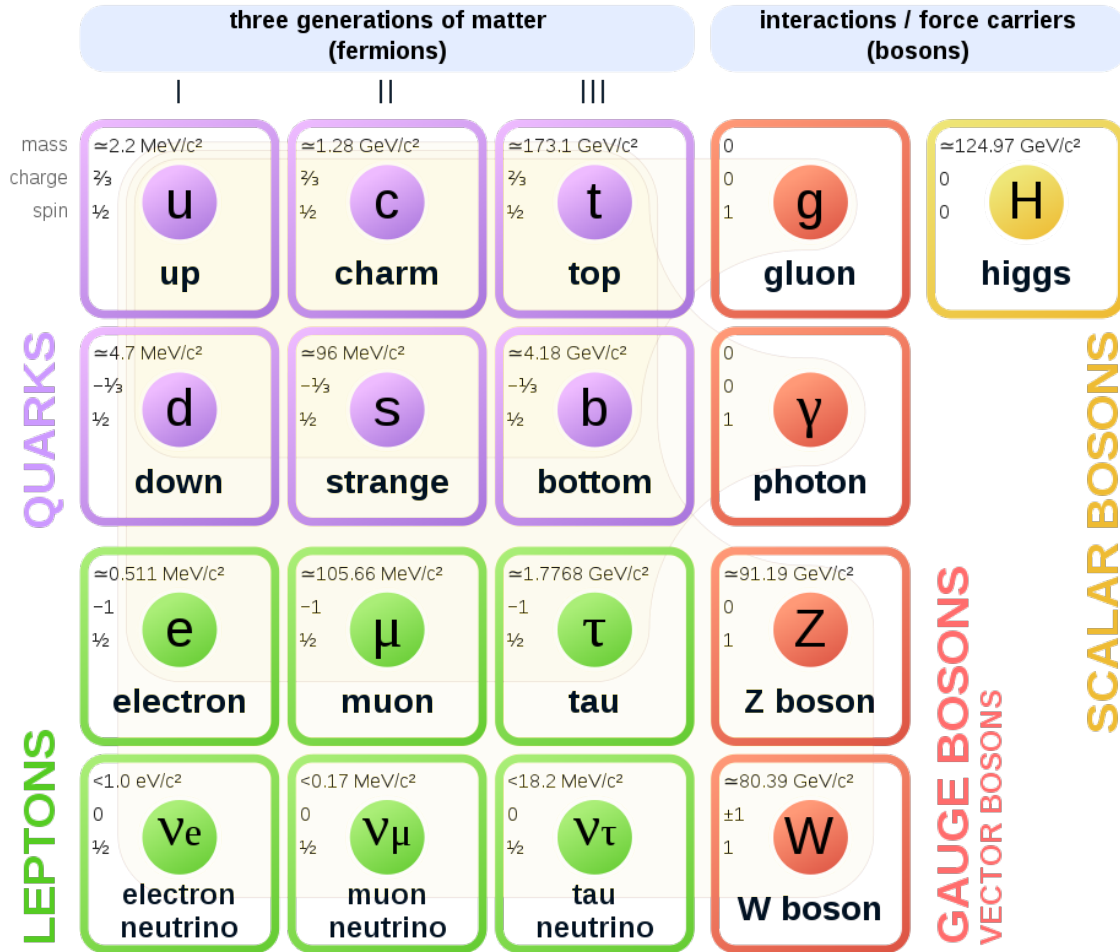
Figure 2.1: *The Standard Model (SM) of particle physics [5]*

down-type quarks and anti-up-type quarks is $-\frac{1}{2}$. The isospin is a flavor quantum number. The flavor indicates the quark contents in a process. Quarks carry a quantum number called color and can not exist as free particles but form composite, observable particles. Two quark states are called mesons (pions, kaons, ...), while three quark states are called baryons (protons, neutrons, ...). Mesons and baryons always have an integer charge. Thus mesons consist of one quark and one anti-quark, while baryons consist either of only quarks or only anti-quarks. Following the additivity of spins, mesons have integer spins

and are therefore bosons while baryons have half integer spins, which makes them fermions.

In the boson group, the gauge bosons are the force mediators. The gluon is the exchange particle of the strong force and the photon is the exchange particle of the electromagnetic force. Both are massless and electrically neutral. The flavor is conserved in electromagnetic and strong interactions, meaning that no transition between the different quark generations is possible. Two massive particles, the Z and the W boson mediate the weak force. While the Z boson has no charge, the W boson can have either a charge of 1 or -1. The Z boson can only couple to fermions of the same flavor. The W boson couples to fermions of different flavor. It carries charge and thus will transform an up-type quark into a down-type quark or vice versa. The transition can also happen between different generations. This is discussed in more detail in section 2.5. All these gauge bosons have a spin of 1 and are therefore called vector bosons. The Higgs boson, which was the last SM particle to be found until 2012, on the other hand has a spin of 0 and is called a scalar boson [6]. It assigns mass to the SM particles.

As described above, the SM fails to incorporate the fundamental force of gravity. In addition to that, the SM fails to explain several more phenomena, like non-zero neutrino masses, Dark Matter and Dark Energy [7]. For this reason, the search for a more complete theory is ongoing. The Belle II experiment is on the frontier of this search for New Physics (NP).

2.2 Discrete Symmetries

The Noether theorem [8] states that every continuous symmetry of a physical system corresponds to a conservation law in that system. This theorem has proven to be one of the most powerful tools of theoretical physics. In the following, discrete symmetries in particle physics are discussed.

Parity Conjugation

The parity conjugation is performed by the parity operator $\hat{\mathcal{P}}$. It mirrors the spatial coordinates of the system in the origin.

$$\hat{\mathcal{P}}\vec{r} = -\vec{r} \tag{2.1}$$

If the parity operator is applied twice to a system, the original system has to result.

$$\hat{\mathcal{P}}^2 \Psi(\vec{r}) = \lambda_{\mathcal{P}}^2 \Psi(\vec{r}) = \Psi(\vec{r}) \tag{2.2}$$

As a consequence, the eigenvalue of the parity operator is $\lambda_{\mathcal{P}} = \pm 1$. The eigenvalue is e.g. $+1$ for axial vectors (they don't change under the conjugation) and -1 for polar vectors.

The spin $\vec{s}$ and angular momentum $\vec{L}$ vectors are axial vectors, while the momentum of a particle $\vec{p}$ is a polar vector. A particle is called right-handed if the momentum and spin vectors point in the same direction and left-handed if they point in opposite directions. For this reason, a parity conjugation switches the handedness of a particle.

Charge Conjugation

The charge conjugation operator $\hat{\mathcal{C}}$ turns a particle in its anti-particle. Thus, it inverts the electromagnetic charge, baryon number, lepton number and flavor [9]. Applying the charge operator twice restores the initial system. Thus, it's eigenvalues are $\lambda_{\mathcal{C}} = \pm 1$. For the eigenvalue to be $+1$, all inverted quantum numbers have to be zero, which applies if a particle is its own anti-particle, e.g. a neutral pion.

Time Conjugation

The time conjugation operator $\hat{\mathcal{T}}$ inverts the time of the system.

$$\hat{\mathcal{T}} t = -t \tag{2.3}$$

This operator also inverts all vectors but no scalars. Time invariant systems behave symmetrically in both time directions.

2.3 Conservation and Violation of Symmetries

2.3.1 The CPT-Theorem

The CPT-theorem lays ground to the following considerations regarding symmetry violations. A CPT conjugation is defined as the subsequent application of the $\hat{\mathcal{C}}$, $\hat{\mathcal{P}}$ and $\hat{\mathcal{T}}$ operators to a system. According to the theorem, the CPT symmetry is conserved in every quantum field theory, which is invariant under Lorentz transformation. Since none of the included operators has influence on the mass or lifetime of a particle, it follows that they are identical for particles and anti-particles. Due to the symmetry of the CPT transformation, all symmetry violations in individual or combined conjugations have to be balanced by violations in the remaining symmetries. [10]

2.3.2 Parity and Charge Violation

No charge or parity violations have been observed in strong or electromagnetic interactions, yet. However, within the SM parity and charge violations are maximally present in the weak interaction. In fact, it has been shown that W-bosons only couple to left-handed neutrinos and right-handed anti-neutrinos in the SM approximation of massless neutrinos. Figure 2.2 shows the transformation of neutrinos using the charge and parity conjugation operators.
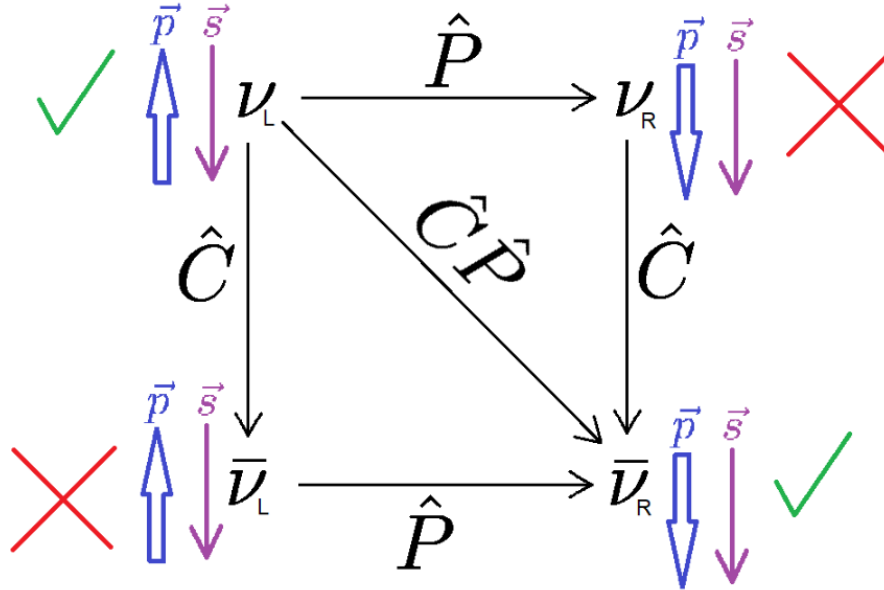
Figure 2.2: *Allowed and forbidden neutrino handedness in the weak interaction and the transformation between the states with the parity and charge conjugation. [11]*

As discussed before, the parity operator changes the handedness of the particles while the charge operator turns the particle into the corresponding anti-particle. The combination of the operators simply does both, so it would e.g. produce a right handed anti-neutrino from a left handed neutrino. Since the weak force does not couple to right-handed neutrinos and left-handed anti-neutrinos, interactions with these particles are forbidden. So far, this observation gives no hint towards a violation of the combined CP conjugation.

2.3.3 CP Violation

CP violation has first been measured by Christenson, Cronin, Fitch and Turlay in 1964 [12]. They used the neutral kaon system of $K^0(d\bar{s})$ and $\bar{K}^0(\bar{d}s)$. These are the flavor eigenstates, since the kaons have been produced in strong interactions, which conserve the flavor. The kaons in turn decay via the weak interaction. At this point, two different neutral kaons K_S and K_L have already been known. The indices "S" and "L" stand for "short" and "long" here, which refers to the significantly different lifetimes of these particles. The individual lifetimes are $\tau_S \approx 9 \times 10^{-11}$s and $\tau_L \approx 5 \times 10^{-8}$s [13]. The even and odd CP eigenstates can be constructed from the flavor eigenstates as follows.

$$|K_1\rangle = \frac{1}{\sqrt{2}} \left(|K^0\rangle - |\bar{K}^0\rangle \right) \tag{2.4}$$

$$|K_2\rangle = \frac{1}{\sqrt{2}} \left(|K^0\rangle + |\bar{K}^0\rangle \right) \tag{2.5}$$

Following this, the CP eigenstates have been identified with the known particles $|K_S\rangle = |K_1\rangle$ and $|K_L\rangle = |K_2\rangle$.

The parity of both flavor kaon eigenstates K^0 and $\bar{K}^0$ is -1. Hence, K_1 is the CP even and K_2 is the CP odd eigenstate. The kaon system can decay into a two pion and three pion final state. The two pion final state is CP even, while the three pion state is CP odd. Thus, if the CP symmetry is conserved, all two pion final states are expected to come from K_1 and all three pion final states have to come from a K_2. To test this, the different lifetimes of the particles have been used. A kaon beam consisting of both known kaons has been created. This beam was lead through a pipe, which was long enough that all K_S^0 particles have decayed at the end and only K_L^0 is left. Then, the final pion states of the decays at the end of the pipe have been examined. Out of 22700 events 45 ± 9 two pion decays have been observed. This proved the violation of the CP symmetry for the first time and was awarded with the nobel price in 1980. This also means that the actual mass eigenstates of the kaon can not be the CP eigenstates introduced before but have to be extended as follows.

$$|K_S\rangle = \frac{1}{\sqrt{1 + |\epsilon|}} \left(|K_1\rangle + \epsilon |K_2\rangle \right) \tag{2.6}$$

$$|K_L\rangle = \frac{1}{\sqrt{1 + |\epsilon|}} \left(|K_2\rangle + \epsilon |K_1\rangle \right) \tag{2.7}$$

Here, ϵ is a CP symmetry breaking factor, which has been measured as $|\epsilon| \approx 2.26 \times 10^{-3}$ [14].

Following the CPT theorem, there also has to be a violation in the time conjugation symmetry due to the CP violation.

2.4 Types of CP Violation

It is known today that a CP violation can have several sources. These sources will be qualitatively discussed in this section. We consider a nonspecific decay, where the initial particle is denoted by X and its anti-particle by $\bar{X}$. Analogously, the final state and its anti-state are denoted by f and $\bar{f}$ and the respective decay amplitudes are A and $\bar{A}$.

Direct CP Violation

A direct CP violation is present, if a decay process and its parity conjugated anti-process appear at different rates.

$$|A_f| \neq |\bar{A}_{\bar{f}}| \tag{2.8}$$

The inequality is displayed in the following figure (2.3).

Figure 2.3: *Illustration of direct CP violation [11]*

The complete amplitude of a decay is the sum of possibly multiple decay contributions, which each have a magnitude A_i, a strong phase δ_i related to the hadrons in the final state f, and a weak phase ϕ_i, which is related to the wekly decaying initial state X. The different contributions will be discussed in more detail in section 4. The total amplitude can then written as

$$A_f = \sum_i A_i e^{i(\delta_i + \phi_i)}. \tag{2.9}$$

Applying a CP transformation to this amplitude only changes the sign of all weak phases ϕ_i. Calculating the difference between the square of the absolute values of the amplitudes yields

$$|A_f|^2 - |\bar{A}_{\bar{f}}|^2 = 2 \sum_{i,j} A_i A_j sin(\phi_i - \phi_j) sin(\delta_i - \delta_j). \tag{2.10}$$

This shows that the difference between the weak and the strong phases must be non-zero for a CP violation to occur. Thus, at least two different weak phases and at least two different strong phases are needed, which means that at least two different amplitudes have to contribute to the decay.

Indirect CP Violation

Neutral mesons, such as B^0 or K^0, can oscillate between the different flavor eigenstates via the weak interaction. This is the case in the neutral kaon system discussed above and the neutral B meson systems, which is investigated in the Belle II experiment. The weak eigenstates can then be formed as a linear combination of the flavor eigenstates. An explicit example for this is given in equations 2.6 and 2.7. If the rate of the transition from the particle to the anti-particle $\Gamma(X \to \bar{X})$ differs from the rate of the inverse process $\Gamma(\bar{X} \to X)$, indirect CP violation occurs. This is also called CP violation in mixing. The inequality is displayed in figure 2.4.

Figure 2.4: *Illustration of indirect CP violation [11]*

CP Violation in the Interference of Mixing and Decay

This type of CPV occurs if both the initial state and its CP conjugated counterpart can decay into the same final state. The violation is a consequence of the interference of the two amplitudes here. The process is shown in figure 2.5.
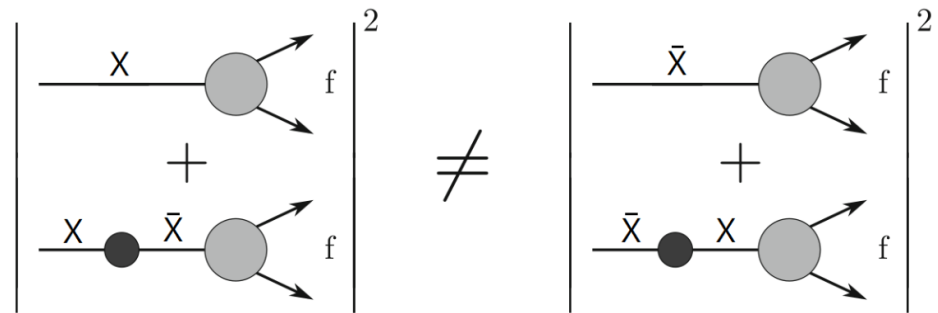
Figure 2.5: *Illustration of CP violation in the Interference of Mixing and Decay [11]*

The time dependence of the oscillations also generates a time dependent CP violation given by

$$\mathcal{A}(t) = \frac{d\Gamma[\bar{X} \to f](t)/dt - d\Gamma[X \to f](t)/dt}{d\Gamma[\bar{X} \to f](t)/dt + d\Gamma[X \to f](t)/dt} \tag{2.11}$$

[15].

2.5 The CKM Matrix

The weak interaction is the fundamental force in the SM mediated via a charged exchange boson, the $W^{\pm}$. For this reason, it can include transitions from an up-type quark to a down-type quark and vice versa. In addition, the generation of the quark can change in the process as well. To explain this mixing, Nicola Cabibbo introduced the Cabibbo-angle θ_C [16], which transforms the mass eigenstate of a quark q to it's weak eigenstate q'. At this time, only the up, down and strange quark were known, but there were already hints

for the existence of the charm quark. In modern notation, the transition matrix looked as follows:

$$
\begin{pmatrix} d' \\ s' \end{pmatrix} = \begin{pmatrix} cos\theta_C & sin\theta_C \\ -sin\theta_C & cos\theta_C \end{pmatrix} \begin{pmatrix} d \\ s \end{pmatrix} = \begin{pmatrix} V_{ud} & V_{us} \\ V_{cd} & V_{cs} \end{pmatrix} \begin{pmatrix} d \\ s \end{pmatrix}
\tag{2.12}
$$

In order to explain the observed CP violation in the kaon system, the 2x2 matrix shown in equation 2.12 has to be enlarged to at least 3x3, consequently a third generation of quarks has to be introduced. This conjecture has been proposed by Kobayashi and Maskawa in 1973 giving the matrix the name Cabibbo-Kobayashi-Maskawa (CKM) matrix [2].

$$
V_{CKM} = \begin{pmatrix} V_{ud} & V_{us} & V_{ub} \\ V_{cd} & V_{cs} & V_{cb} \\ V_{td} & V_{ts} & V_{tb} \end{pmatrix}
\tag{2.13}
$$

Here, the individual entries of the matrix are the transition probabilities between the quarks. In general, these are complex numbers, giving the matrix 18 degrees of freedom. Since the SM assumes that only three generations of quarks exist and the quark has to make any transition when a W-boson is involved, this matrix has to be unitary. By using the constraints of the unitarity and removing physically irrelevant phases the matrix can be expressed using four degrees of freedom. Most commonly used is the Wolfenstein parametrization [17].

$$
V_{CKM} = \begin{pmatrix} 1 - \frac{1}{2}\lambda & \lambda & A\lambda^3(\rho - i\eta) \\ -\lambda & 1 - \frac{1}{2}\lambda & A\lambda^2 \\ A\lambda^3(1 - \rho - i\eta) & A\lambda^2 & 1 \end{pmatrix} + \mathcal{O}(\lambda^4)
\tag{2.14}
$$

Here, the Cabibbo angle appears as $\lambda = sin\theta_C \approx 0.23$. It can be seen in equation 2.14 that the transitions within one generation (diagonal elements) have a probability of almost 1. In general, the probability of the considered transition is roughly given by the leading power of λ.

Using the unitarity condition

$$
\sum_{k=1}^{3} V_{ik}^* V_{kj} \overset{!}{=} 0 \quad (i, j = 1, 2, 3 \mid i \neq j)
\tag{2.15}
$$

the following explicit constraints can be stated.

$$
V_{ud}V_{us}^* + V_{cd}V_{cs}^* + V_{td}V_{ts}^* = 0
\tag{2.16}
$$

$$
V_{ud}V_{ub}^* + V_{cd}V_{cb}^* + V_{td}V_{tb}^* = 0
\tag{2.17}
$$

$$V_{us}V_{ub}^* + V_{cs}V_{cb}^* + V_{ts}V_{tb}^* = 0 \tag{2.18}$$

These can be displayed as triangles in the complex plane. When looking at the Wolfenstein parametrization it can be seen that relation 2.17 is the only one in which all contributions are of the same order ($\mathcal{O}(\lambda^3)$). Thus, it is expected that the angles of the triangle are fairly even. The triangle for this condition in the complex plane normalized to $V_{cd}V_{cb}^*$ is displayed in figure 2.6.
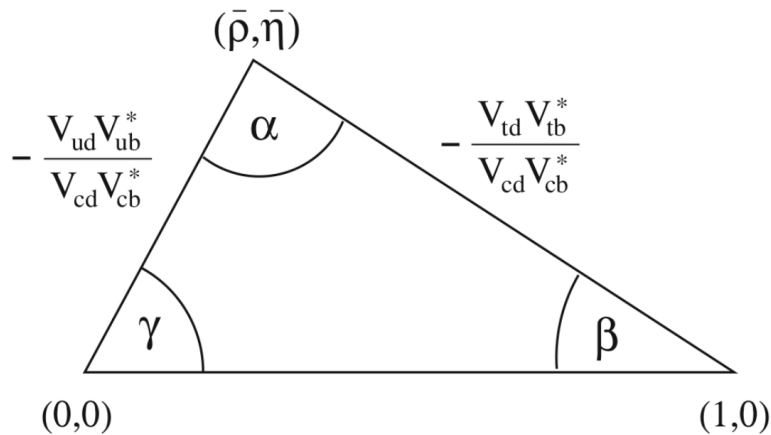
Figure 2.6: *Unitarity triangle for equation 2.17 normalized to $V_{cd}V_{cb}^*$ [15]*

Here, the angles are given as

$$\alpha = arg\left(-\frac{V_{td}V_{tb}^*}{V_{ud}V_{ub}^*}\right), \quad \beta = arg\left(-\frac{V_{cd}V_{cb}^*}{V_{td}V_{tb}^*}\right), \quad \gamma = arg\left(-\frac{V_{ud}V_{ub}^*}{V_{cd}V_{cb}^*}\right) \tag{2.19}$$

and $\bar{\rho}$ and $\bar{\eta}$ are introduced as

$$\bar{\rho} = \rho\left(1 - \frac{\lambda^2}{2}\right), \quad \bar{\eta} = \eta\left(1 - \frac{\lambda^2}{2}\right) \tag{2.20}$$

The SM can be examined by measuring the angles and sides of the triangles. If any triangle is not closed it is a hint for NP. The comparable angles in the triangle depicted in figure 2.6 create a larger area than for the other constraints. This makes this constraint particularly interesting. Two sides and all three angles of the shown triangle can be determined from B decays. This overconstrains the triangle and makes a check on the SM feasible.

The current combined global status of the measurements is displayed in figure 2.7.
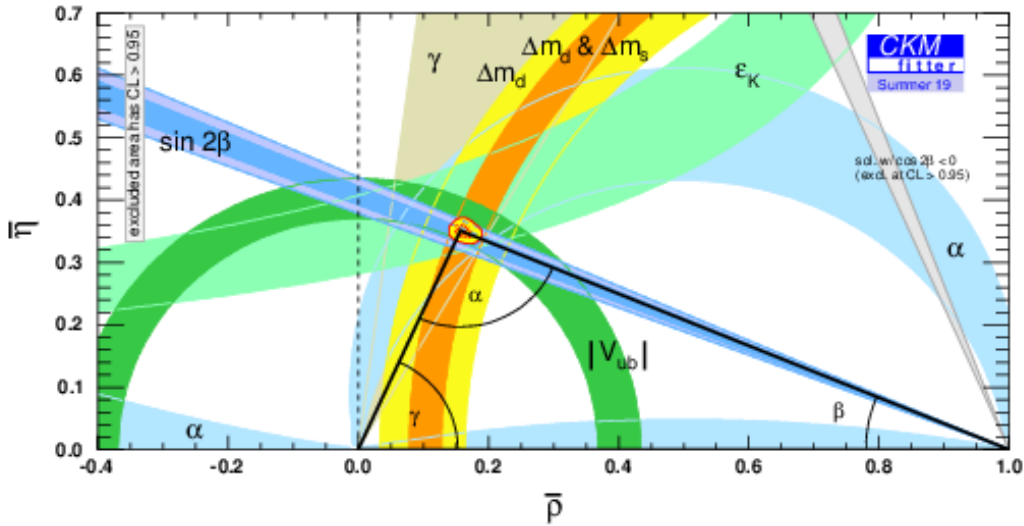
Figure 2.7: *Global CKM fit in the $(\bar{\rho}, \bar{\eta})$ plane [18]*

2.6 B Production and Tagging

Next to the large angles of the unitarity triangle, the B meson system has further physical advantages. One such advantage is the long lifetime of the neutral B meson system. This makes it easier to study the time dependent CP violation. In addition, by using electron-positron colliders running at specific energies, such as the $\Upsilon(4S)$ resonance, the B mesons can be produced exclusively in pairs, without pollution from other particles unlike in hadron colliders. This simplifies the detection and analysis of the individual events. In addition, the B mesons are produced in an entangled state, which is used in the flavor tagging process. In the following, the production mechanism and the flavor tagging in Belle II will be discussed.

2.6.1 B Meson Production

At Belle II the $B\bar{B}$-pairs are produced via the $\Upsilon(4S)$ resonance. This is an exited state of the Υ particle, a bound $b\bar{b}$ state. In general, mesons consisting of a heavy (c or b) quark and its anti-particle ($q\bar{q}$) are called quarkonium states. This $\Upsilon(4S)$ resonance is chosen because it has just enough mass to produce two B mesons. Hence, exclusive $B\bar{B}$ states are produced without any additional particles. The Feynman diagram of the production mechanism is shown in figure 2.8.

In addition, all $q\bar{q}$ pairs consisting of lighter quarks than the b quark (up, down, charm, strange) can be produced in the electron-positron collision. These events are summarized
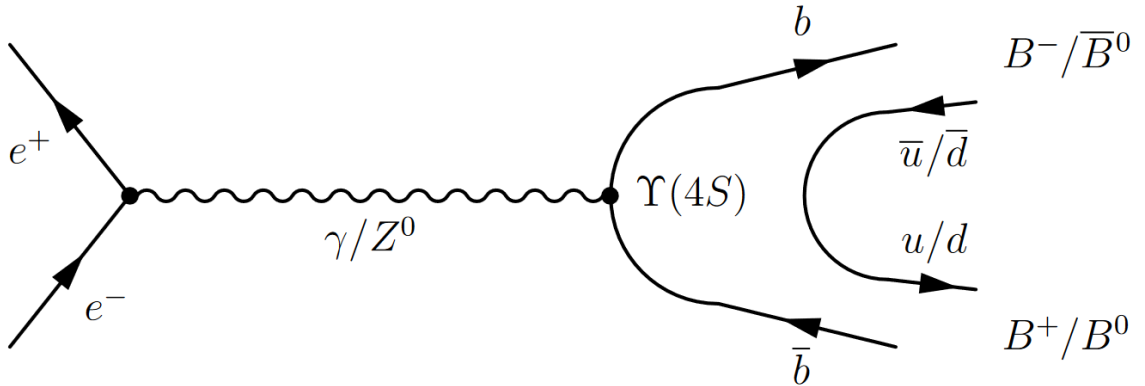
Figure 2.8: *Feynman diagram of the B meson pair production via the $\Upsilon(4S)$ resonance as done at Belle II [9]*

as continuum background. The cross section ratio of the continuum events and the production of a $\Upsilon(4S)$ is about $3:1$. From the $\Upsilon(4S)$, a $B\bar{B}$ pair is produced in more than 96% of the cases [19]. The production of B^+B^- and $B^0\bar{B}^0$ pairs is expected to be even with a ratio of $\Gamma(B^+B^-)/\Gamma(B^0\bar{B}^0) \approx 1.06 \pm 0.03$ [19].

2.6.2 Flavor Tagging

The two produced B mesons are in an entangled P-wave due to the conservation of angular momentum. In the case of a $B^0\bar{B}^0$ pair the mesons will oscillate but they do so in a coherent way before any of them decays. Measuring the flavor of one particle immediately determines the flavor of the second one to be opposite at this point in time. The flavor is identified at the moment of the decay of the first particle t_{tag}. Then, the second particle can oscillate until its decay at t_{CP}. The difference of the decay times $\Delta t = t_{CP} - t_{tag}$ and the individual B flavors at the decay time are used for the determination of time dependent CP violation parameters. Unfortunately the time difference Δt is too small to be measured by timing devices, such as fast scintillators. For this reason, the decay positions are measured. Using the boost of the system, which comes from different particle energies, the decay time differences can be calculated from the decay length. A sketch of this procedure is shown in figure 2.9.
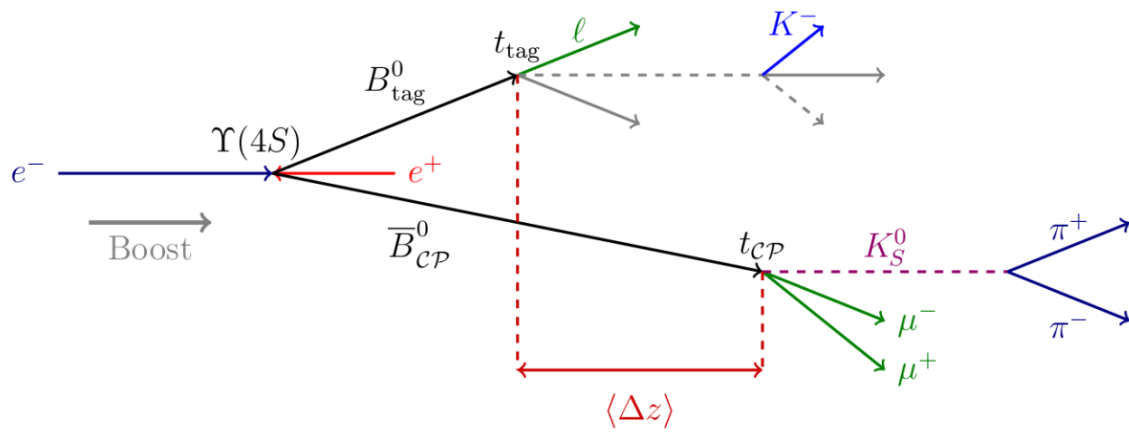
Figure 2.9: *Sketch of the tagging procedure used for the neutral B meson system. The decay time difference is determined by the spatial distance of the decays and the boost of the system [11]*

3 The Belle II Experiment

For a significant measurement of the time dependent CP violation, the Belle II detector has to be able to measure the distances between the B meson decays with high precision. Belle II and SuperKEKB are designed to produce the most precise measurements in B physics to date. In order to do so, a new sub-detector, the Pixel Vertex Detector (PXD), has been introduced within the upgrade from Belle to Belle II. In the following, the upgraded accelerator SuperKEK B factory (KEKB) and the Belle II detector, including all sub-detectors are introduced.

3.1 SuperKEKB

The SuperKEKB accelerator is an electron positron collider, which mainly operates on the center-of-mass energy $\sqrt{s}$ of 10.58GeV. This corresponds to the resonance of the $\Upsilon(4S)$. The collider has two separate rings, the High Energy Ring (HER) for the electrons and the Low Energy Ring (LER) for the positrons. The respective beam energies are 7GeV and 4GeV. This results in an overall boost of $\beta\gamma = 0.28$ of the system. In comparison to the previous accelerator, the KEKB, the SuperKEKB is designed to achieve a much higher luminosity. A sketch of the detector is shown in figure 3.1.

While KEKB set a world record with a peak luminosity of $2.108 \times 10^{34} \mathrm{cm}^{-2}\,\mathrm{s}^{-1}$, SuperKEKB aims for a peak instantaneous luminosity of $\mathcal{L} = 6 \times 10^{35} \mathrm{cm}^{-2}\,\mathrm{s}^{-1}$, which would be an improvement of almost a factor of 30. The instantaneous luminosity is related with the collision rate dN/dt for a certain process with cross section σ_P in the detector by

$$\frac{\mathrm{d}N}{\mathrm{d}t} = \sigma_P \cdot \mathcal{L}, \tag{3.1}$$

where $\mathcal{L}$ denotes the instantaneous luminosity. The luminosity depends on several factors and can be expressed as

$$\mathcal{L} = \frac{N_{e^+} N_{e^-} f_c}{4\pi \sigma_x \sigma_y} R_L. \tag{3.2}$$

Here, N_{e^+} and N_{e^-} denote the number of particles in the colliding electron and positron bunches, respectively. f_c is the bunch collision frequency and σ_x, σ_y are the root mean squares of the transverse beam size at the collision point. R_L as the last factor is a luminosity reduction factor depending on various variables. It is designed to be $R_L = 0.86$ [21].
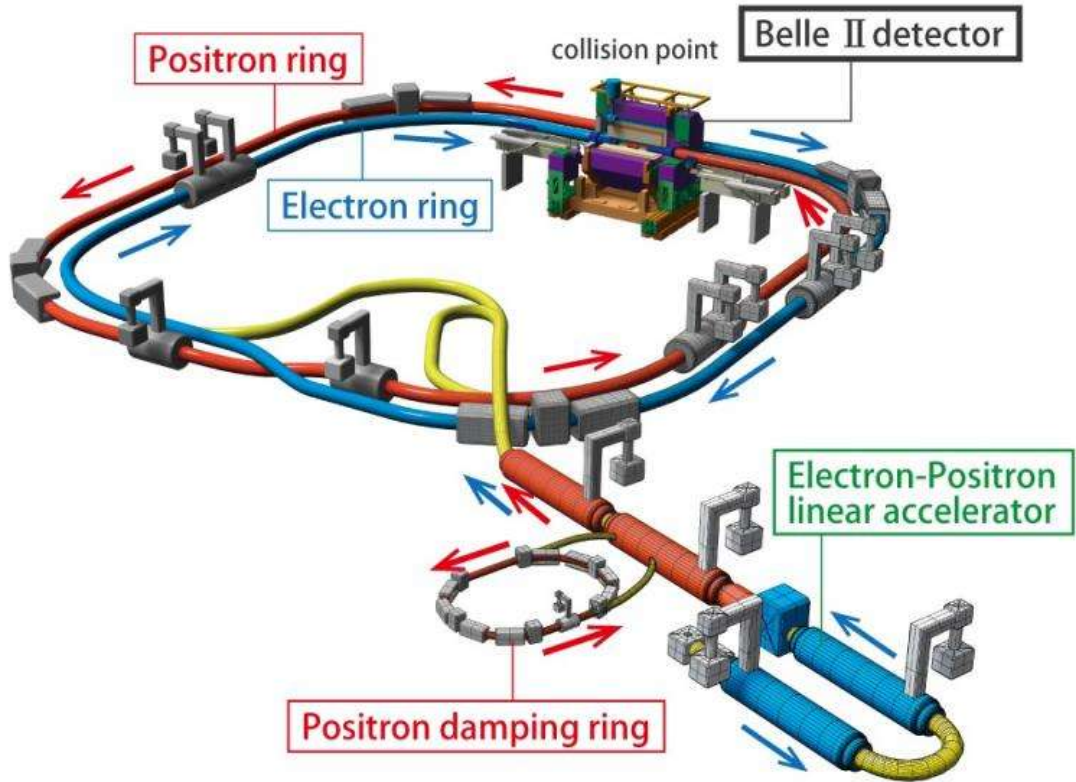
Figure 3.1: *Illustration of the SuperKEKB accelerator [20].*

Following equation 3.1 the total number of events for a given cross section σ_P can be calculated by the integration over time. This also motivates the physical quantity of the integrated luminosity $\mathcal{L}_{int}$.

$$N = \sigma_P \int\limits_{t_0}^{t_1} \mathcal{L} = \sigma_P \mathcal{L}_{int} \tag{3.3}$$

It follows from equation 3.3 that the number of recorded events is directly proportional to the integrated luminosity. For that reason, the size of a data set is given by the integrated luminosity.

Initially, SuperKEKB was designed for a peak luminosity of $\mathcal{L} = 8 \times 10^{35} \mathrm{cm}^{-2}\,\mathrm{s}^{-1}$. In order to achieve the 40-fold increase in luminosity compared to KEKB, $\sigma_x \sigma_y$ shall be decreased by a factor of 20. The reduction of the beam widths at the Interaction Point (IP) shall be achieved with the introduction of the so-called nano-beam scheme. Here, the beam is squeezed by focusing superconducting quadrupoles at the IP. In addition to

that, the beam currents are doubled in the new setup. A more detailed discussion of the accelerator can be found in Akai, Furukawa, and Koiso [22].

3.2 The Belle II Detector

This increase in the instantaneous luminosity also sets new requirements for the detector. Belle II has to be able to cope with the higher frequency of events as well as higher background rates. In addition, the trigger scheme, data acquisition system and computing had to be upgraded due to the increasing data rate with the higher event rates.

The different subdetectors of Belle II are arranged in an onion like shell structure around the beam pipe. In total, almost the full solid angle is covered and the combination of the data from all sub detectors allows for an efficient particle identification and precise measurements on their tracks, momenta and energies. The full detector can be seen in figure 3.2.
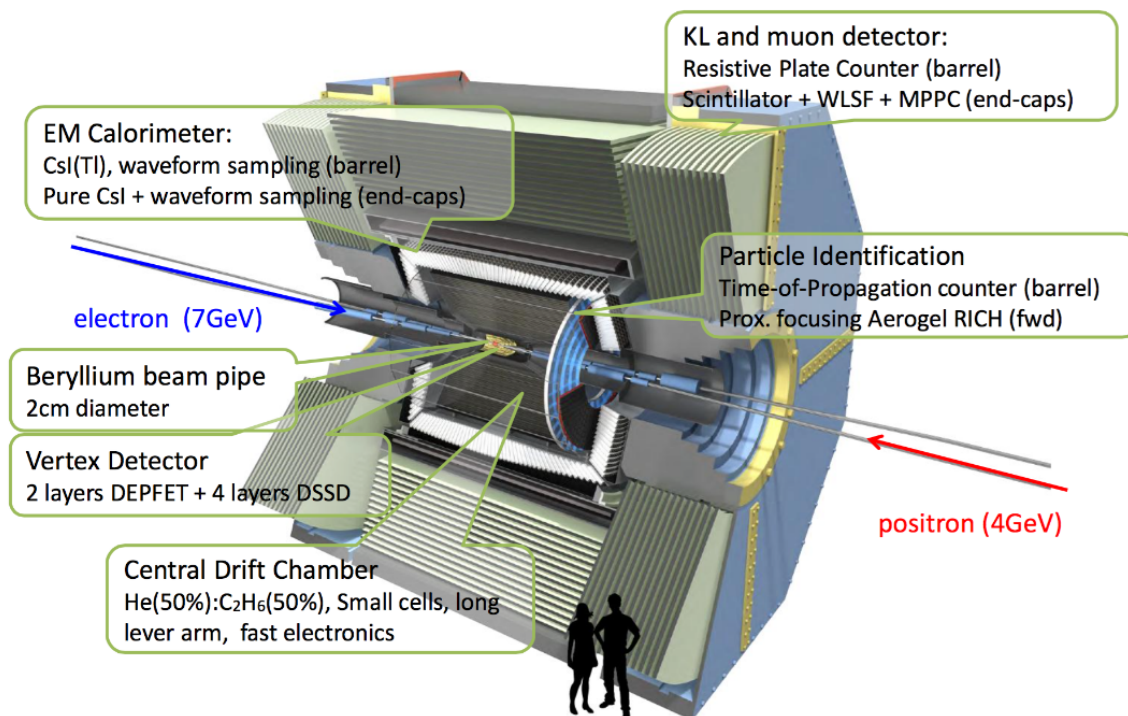
Figure 3.2: *Animation of the Belle II detector with the individual sub detectors [23].*

In this section, the individual sub detectors starting with the innermost component are introduced.

3.2.1 Vertex detector (VXD)

The VXD consists of two sub detectors, the Pixel Vertex Detector (PXD) and the Silicon Vertex Detector (SVD). The PXD is made of two layers of DEpleted P-channel Field Effect Transistors (DEPFETs) pixels at the radii $r = 14$mm and $r = 22$mm. These are the innermost detector parts and are placed directly on the beryllium beam pipe. The PXD significantly improves the accuracy of the track measurement and thus improves the vertex resolution. The second component, the SVD, adds four layers of double sided silicon strip sensors at the radii 38mm, 80mm, 115mm, and 140mm around the beam pipe to that. These silicon strips detect passing particles with an angular acceptance of $17° < \theta < 150°$.
In combination with the Central Drift Chamber (CDC), the VXD reconstructs the origins of the particles. In addition, the particle momenta can be measured using the curvature of the particle trajectory in solenoid magnetic field, which will be discussed later. The VXD has a spatial precision along the beam pipe of $\sigma(d_z) \approx 20$µm and can reconstruct particles with transverse momenta above $p_t \approx 30$MeV$/c$. [9]

3.2.2 Central Drift Chamber (CDC)

The CDC measures the momenta of charged particles and the energy loss of particles, which is important for the particle identification. The CDC is arranged around the VXD in 56 cylindrical wire layers with an inner radius of 16cm and an outer radius of 113cm, which is bigger than in Belle. This chamber is filled with a gas mixture containing 50% helium and 50% ethane. In this environment, 14336 sense wires and 42240 field wires have been installed. Each sense wire is surrounded by eight field wires forming one complete rectangle. The field wires create an electrical field, which accelerates electrons towards the sense wires. These free electrons are created by charged particles passing the chamber and ionizing the gas. While the electrons move towards the sense wire they ionize again and create an electron avalanche, which can then be detected as a signal. The wires form nine superlayers in the detector. Five of them are axial, which means that all wires in this layer are oriented along the z-axis of the cylindrical detector giving the polar coordinates of the hit. In order to allow for a 3D reconstruction, four stereo layers are interspersed between the axial layers, with the wires skewed with respect to the z-axis. The axial and stereo superlayers are arranged in an alternating way. The resulting spatial resolution of the CDC is 100µm. [24]

3.2.3 Cherenkov Detectors

In order to improve the particle identification, two new sub detector using the Cherenkov effect have been introduced in Belle II. Their main task is the differentiation between charged kaons and charged pions. If one of those mesons, or any charged particle, passes a dielectric medium with a velocity, greater than the speed of light in that medium they

radiate photons. The angle of these Cherenkov photons solely depends on the velocity of the particle. By combining this information with the momentum measurement, the mass of the particle can be extracted and the particle can be identified. One detector using this principle in Belle II is the Aerogel Ring-Imaging CHerenkov Detector (ARICH). It is located in the forward endcap direction covering a polar angle of 17° to 35°. Here, an aerogel radiator where the Cherenkov light is produced is placed in front of photon detectors. This is complemented by the Time of Propagation detector (TOP) detector, covering a polar angle of 32° to 120°. It consists of totally reflecting quartz bars. The Cherenkov light produced in the bars is thus directed to the end of the bar where a photon detector is installed. Next to the velocity of the particle, a precise time measurement is enabled by the fast sensor time resolution of about 100ps [25]. The working principle of both detectors is illustrated in figure 3.3. [24]
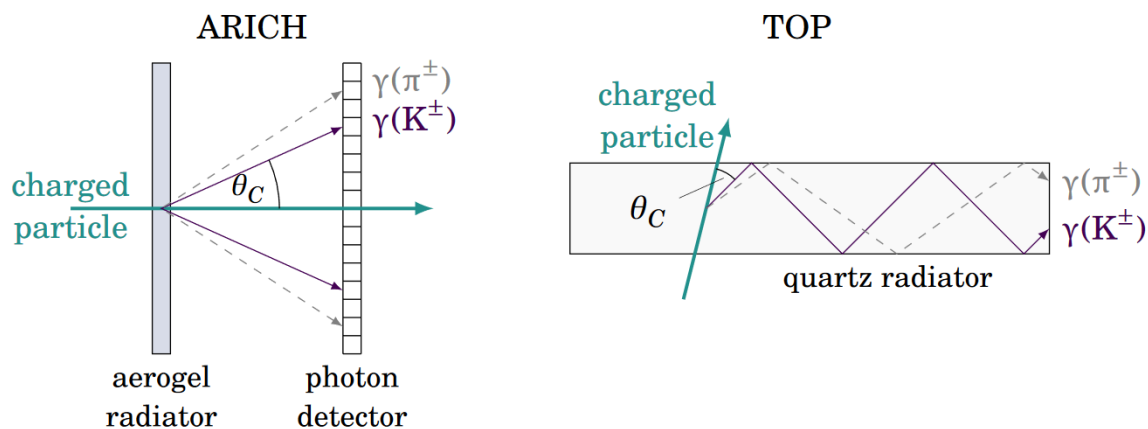
Figure 3.3: *Working principle of the ARICH and TOP sub detectors. [24]*

3.2.4 Electromagnetic Calorimeter (ECL)

Photons are detected in the ECL. Here, their energy and position are measured. In addition, the ECL identifies electrons and is a part of the first level trigger. The detector is split up into a barrel region around the IP as well as a forward and a backward region at the end caps. In total, it consists of 8736 thallium-doped caesium iodide scintillation crystals. Incoming photons create electron positron pairs in the crystal, which emit bremsstrahlung photons again leading to the repetition of this process. This leads to a particle shower until the energy of the photons is too low to create additional electron positron pairs. These slow electrons and positrons then create light in the crystals, which is measured.

3.2.5 Solenoid Magnet

Around the ECL, a superconduction solenoid is placed with a radius of 1.7m and a length of 4.4m. This solenoid creates a magnetic field of 1.5T, which bends the trajectories of charged particles in the detector. Using the curvature of the trajectories determined by e.g. the CDC allows for a momentum measurement.

3.2.6 K_L and μ detector (KLM)

As the name suggests, the K_L and μ detector (KLM), which is the outermost detector, has the task to detect long lived kaons and muons. It consists of alternating layers of 4.7cm thick iron plates and active detector elements. The two inner layers of active detector elements and the elements in the endcaps are scintillator strips, since these can withstand high event and background rates. The other elements are glass-electrode resistive plate chambers (RPCs). Muons create tracks in these active detector elements, which can be paired with tracks from the CDC. Muons are expected to pass all active detector elements, which can distinguish them from charged hadrons. Long lived kaons produce hadronic showers in the KLM. These can then be combined with the signal in the ECL from the kaon.

4 Theory Parameters of $B \to K^{(*)}\pi$ Decays

The set of $B \to K^{(*)}\pi$ decays is particularly interesting, because the decays are mediated by gluonic penguin diagrams in the leading order due to the strong suppression of the $b \to u$ transition on the tree level. This makes these decays sensitive to NP contributions in the penguin loops. The existing measurements of the branching ratios and CP asymmetries of the $B \to K^{(*)}\pi$[1] decays give information about the strengths of the different contributing decay amplitudes. This also gives insights into the impact of the respective measurements and their errors on the theory parameters. The so-called $K\pi$-Puzzle can be visualized and important new measurements from Belle II can be identified. In addition to that, one can see which amplitudes are important to explain the current experimental status and which can be neglected for now.

The theoretical introduction to this chapter is largely based on Beaudry et al. [26][2].

4.1 Theory and Procedure

4.1.1 $B \to K^{(*)}\pi$ Decay Amplitudes

Following a diagrammatic approach, decays of the B into two mesons $B \to M_1 M_2$ can be categorized by a set of different transition diagrams (or amplitudes) for the different flavor topologies of the decay [27]. The most important decay diagrams are shown in figure 4.1. Each of these diagrams has a distinct amplitude with magnitude and strong phase, which can be treated individually. The important transition amplitudes for the $B \to K^{(*)}\pi$ decays have been found to be the color allowed and suppressed tree diagrams T' and C', the gluonic penguin diagram P', and the electroweak penguin diagram and it's color suppressed counterpart P'_{EW} and P'^C_{EW}. The exchange E', flavor-singlet penguin S', annihilation A' and penguin-annihilation PA' diagrams are neglected here, since they are expected to be very small for these decays [26]. The annihilation diagram is missing in

---

[1] K^* refers here and in the following to $K^*(892)$

[2] In this paper, the Pion is always named first, while the Kaon is the second particle. Since it is more common to name the Kaon first, all information from Beaudry et al. [26] and other sources using the different notation has been adjusted. Following this notation, e.g. the abbreviation (+0) stands for $K^+\pi^0$ here.
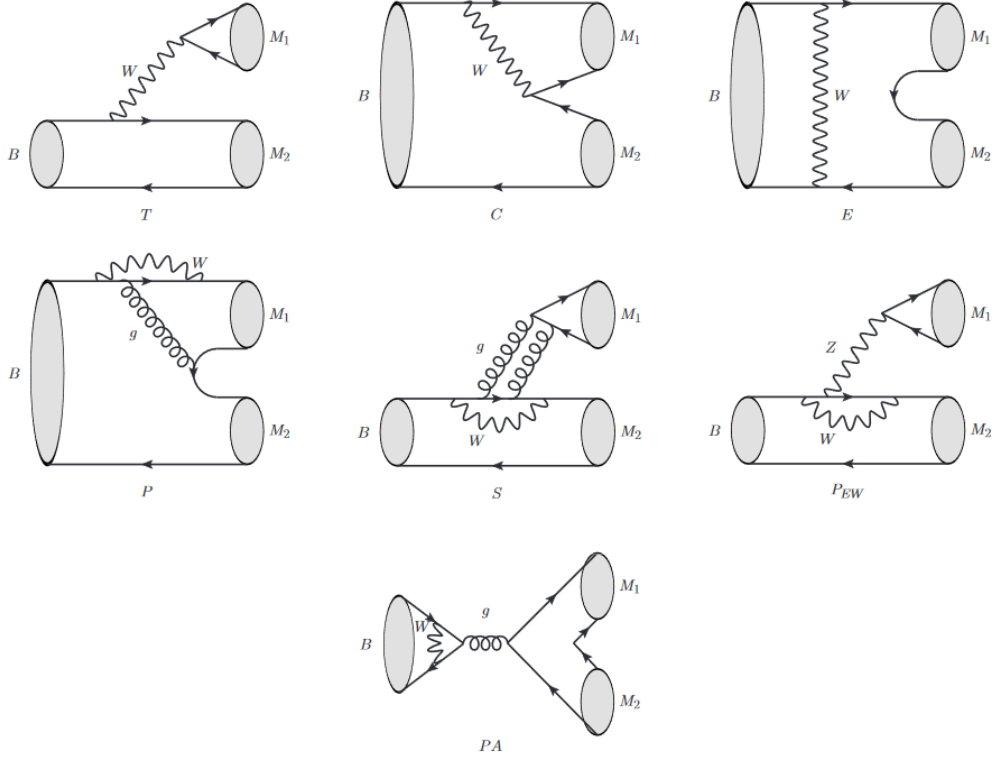
Figure 4.1: *Most important $B \to M_1 M_2$ decay diagrams by flavor topology classification. [25]*

figure 4.1, since it is helicity suppressed[3].

The gluonic penguin diagram P' can be split up into three contributions for the possible quarks in the loop. These can be narrowed down to two components by using the unitarity condition of the CKM matrix ($V_{ub}^* V_{us} + V_{cb}^* V_{cs} + V_{tb}^* V_{ts} = 0$) as follows:

$$
\begin{aligned}
P' &= V_{ub}^* V_{us} P_u' + V_{cb}^* V_{cs} P_c' + V_{tb}^* V_{ts} P_t' \\
&= V_{ub}^* V_{us}(P_u' - P_c') + V_{tb}^* V_{ts}(P_t' - P_c')
\end{aligned}
\tag{4.1}
$$

With the definitions $P_{tc}' \equiv |V_{tb}^* V_{ts}|(P_t' - P_c')$ and $P_{uc}' \equiv |V_{ub}^* V_{us}|(P_u' - P_c')$ only these two contributions remain. Their strengths can be related using the CKM matrix elements as $P_{tc}' \sim \lambda^2$ and $P_{uc}' \sim \lambda^4$. This can be done analogously for the electroweak penguin amplitudes. However, $P_{EW}'^C$ is expected to be very weak and will thus not be considered in such detail and P_{EW}' can be approximated using the color allowed tree diagram, which

---

[3]The prime on the amplitudes states that it is a strangeness changing decay. This is always the case in this thesis, but this notation is adopted to maintain a consistency with other papers on this subject.

is more convenient for the fit. Now, the remaining amplitudes can be roughly arranged by their expected magnitudes [26].

$$\text{1.Order: } |P'_{tc}| \quad \text{2.Order: } |T'|, |P'_{EW}| \quad \text{3.Order: } |C'|, |P'_{uc}|, |P'^C_{EW}|$$

The decay amplitudes of the various considered $B \to K^{(*)}\pi$ decays can then be calculated using these different contributions. The decay amplitudes of the $B \to K^{(*)}\pi$ decays are given by [26]:

$$A^{0+} = -P'_{tc} + P'_{uc}e^{i\gamma} - \frac{1}{3}P'^C_{EW} \tag{4.2}$$

$$\sqrt{2}A^{+0} = -T'e^{i\gamma} - C'e^{i\gamma} + P'_{tc} - P'_{uc}e^{i\gamma} - P'_{EW} - \frac{2}{3}P'^C_{EW} \tag{4.3}$$

$$A^{+-} = -T'e^{i\gamma} + P'_{tc} - P'_{uc}e^{i\gamma} - \frac{2}{3}P'^C_{EW} \tag{4.4}$$

$$\sqrt{2}A^{00} = -C'e^{i\gamma} - P'_{tc} + P'_{uc}e^{i\gamma} - P'_{EW} - \frac{1}{3}P'^C_{EW} \tag{4.5}$$

These equations are the same for the $B \to K\pi$ and the $B \to K^*\pi$ decays but the individual contributing diagrams can have different strengths and phases for the two cases. There is one complete set of measurements for the $B \to K\pi$ final states containing two pseudoscalar mesons (PP) and a measurement set for the $B \to K^*\pi$ final states of one vector and one pseudoscalar meson (VP). The amplitudes for the CP-conjugated decays result when the sign of the weak phase γ is changed. Each contributing diagram has a modulus and a strong phase which are both included in the term (e.g. $C' = C'_0 e^{i\delta_{C'}}$). It can be easily seen, that these equations follow the isospin sum rule [26]:

$$\sqrt{2}A^{00} + A^{+-} = \sqrt{2}A^{+0} + A^{0+} \tag{4.6}$$

4.1.2 The $K\pi$-puzzle

The two decays $B^0 \to K^+\pi^-$ and $B^+ \to K^+\pi^0$ only differ by a spectator quark in the B meson. The leading decay diagrams of the $B \to K\pi$ system, the color allowed tree and gluonic penguin amplitude, are displayed in detail for the decay $B^0 \to K^+\pi^-$ in figure 4.2.

Replacing the spectator down quark in the neutral B meson in figure 4.2 by an up quark results in the diagrams for the $B^+ \to K^+\pi^0$ decay. Due to this similarity in the leading amplitudes the measured asymmetries in these channels were naively expected to be the same. However, experiments showed $\Delta A_{CP} = A_{CP}(K^+\pi^0-) - A_{CP}(K^+\pi^-) = 0.114 \pm 0.014$ [13]. This unexpected difference is known as the $K\pi$-puzzle. [28] Due to
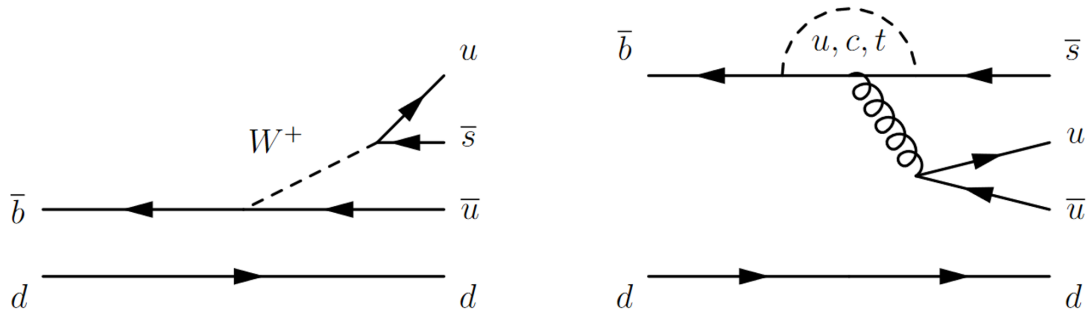
Figure 4.2: *Feynman diagrams of the color allowed tree and gluonic penguin decay diagrams for the $B^0 \to K^+\pi^-$ decay. [28]*

the different spectator quarks in the two modes, different non-leading decay diagrams appear in the two decay modes (see equations 4.3 and 4.4). This difference could lead to an explanation for the $K\pi$-puzzle.

4.1.3 Measured Quantities

Using the given amplitudes, the theoretical branching fraction for a two body decay is given by [29]:

$$BR = \frac{\tau p}{8\pi m^2}|A|^2 \tag{4.7}$$

Here, τ denotes the lifetime of the decaying particle (the B meson in our case). p is the momentum of the final state particles in the rest frame of the decaying particle, and m is the mass of the decaying particle. The direct CP asymmetry of the considered decay can be calculated following the definition of the PDG [13]:

$$A_{CP} = \frac{BR(\bar{B} \to \bar{f}) - BR(B \to f)}{BR(\bar{B} \to \bar{f}) + BR(B \to f)} \tag{4.8}$$

The final state is denoted by the f here, where $\bar{f}$ indicates the CP-conjugated final state. The decaying particle in the discussed decays and its CP counterpart here are the B^+ and the B^- respectively. The mixing induced CP asymmetry S_{CP}, which is only present in the $B^0 \to K^0\pi^0$ channel, can then be calculated via [30]:

$$S_{CP} = sin(2\beta)\sqrt{1 - A_{CP}^2} \tag{4.9}$$

S_{CP} only depends on the CKM angle β and the direct CP asymmetry here.

In addition to the isospin sum rule, the asymmetry sum rule parameter $I_{K\pi}$ is expected to be small within the SM [25].

$$I_{K\pi} = A_{CP}^{+-} + A_{CP}^{0+} \frac{BR(0+)}{BR(+-)} \frac{\tau_{B^+}}{\tau_{B^0}} - 2A_{CP}^{+0} \frac{BR(+0)}{BR(+-)} \frac{\tau_{B^0}}{\tau_{B^+}} - 2A_{CP}^{00} \frac{BR(00)}{BR(+-)} \quad (4.10)$$

An outline of the derivation, which motivated the assumption that $I_{K\pi}$ is small following Gronau and Rosner [31] is given in section 7.

4.1.4 Simplifications and Approximations

The formulae above can be used to calculate theoretical predictions for the measured quantities using only the magnitudes and phases of the contributing diagrams and the prefactors of the decay topology for the BR calculation. Since only the relations between the strong phases are relevant, one of them can be chosen freely. For the following calculations, the strong phase of the tree diagram is set to zero $\delta_{T'} = 0$. Thus, all other strong phases are relative to the strong phase of this diagram. Using this definition, the individual contributions in the amplitude equations can be written for example as $T' = T_0' = |T'|$ and $P_{tc}' = P_{tc_0}' e^{i\delta_{P_{tc}'}}$, where $\delta_{P_{tc}'} = \delta_{P_{tc}'-T'}$. The other contributions follow analogously.

In addition to that, following Beaudry et al. [26], the electroweak penguin amplitude in the $K\pi$ system can be approximated as

$$P_{EW}' = \frac{3}{2} \frac{c_9}{c_1} R T', \quad (4.11)$$

where the analogue approximation can be made for the color suppressed counterparts. Here, c_i are Wilson coefficients. Their respective values are $c_1 = 1.144$ and $c_9 = -\frac{1.28}{129}$. R is defined as

$$R \equiv \left| \frac{V_{tb}^* V_{ts}}{V_{ub}^* V_{us}} \right|. \quad (4.12)$$

This approximation holds within a few percent, which is acceptable since the current state of the measurements only allows for a qualitative description of the decay amplitudes magnitudes. Following Gronau [32], a similar relation holds within a few percent in the $K^*\pi$ system. In order to achieve a good quantitative extraction of values, more precise measurements are needed. [26]

4.1.5 Fitting Method

Using the actual measurements of the decay parameters and the above calculations, the theory parameters which match best with the current experimental status can be found. To do this, a maximum likelihood approach has been chosen here. A Gaussian curve around the measured value with the standard deviation error has been chosen as probability function for each individual estimated measurement. The product of all

individual probability functions gives the overall likelihood in dependence on the free parameters. Thus, more precise measurements give stronger constraints on the parameters. Maximizing the total probability function is equal to minimizing the least squares value χ^2 in the following equation.

$$\chi^2 = \sum_i \frac{(\mathcal{O}_i^{th} - \mathcal{O}_i^{exp})^2}{(\Delta\mathcal{O}_i)^2} \tag{4.13}$$

Here, the theoretical prediction for each measured value, which depends on the parameter set, is $\mathcal{O}_i^{th}$, while the actual measurement value and its experimental error are denoted as $\mathcal{O}_i^{exp}$ and $\Delta\mathcal{O}_i$, respectively. [26]

The general set of free parameters is denoted as $\vec{\theta}$ and the optimal values are $\hat{\vec{\theta}}$. The uncertainties on the optimal fit values are calculated by varying an individual fit parameter until the χ^2 increases by one. All other parameters are constant in this process. This follows from formula 4.14 for $z\sigma$ uncertainties. If the lower and upper errors differ, the bigger one is chosen. [33]

$$\chi^2(\vec{\theta}') = \chi^2_{min} + z^2 \tag{4.14}$$

The achieved minimal χ^2 value is also a measure of the quality of the fit. For a good fit, the ratio of χ^2 and the degrees of freedom $(d.o.f.)$ should be roughly one. Here, the number of degrees of freedom (n) is given by the number of fit points (the number of used measurements in this case) subtracted by the number of floating parameters in the set $\vec{\theta}$ [33]. If this value is very large, it means that the model is unable to fit the measured results within the given errors. On the other hand, if the value gets very small it means that the applied model has too many free parameters and can thus fit the prediction arbitrarily close to the measured value. [26]

The goodness-of-fit can be evaluated more precisely by the p-value. Starting from the χ^2 probability distribution function, which is given as

$$P(\chi^2) = \frac{1}{2^{n/2}\Gamma(n/2)}(\chi^2)^{(n/2-1)}e^{-\chi^2/2}, \tag{4.15}$$

the p-value can be calculated to be

$$p = \int_{\chi^2_{min}}^{\infty} P(\chi^2)\,\chi^2. \tag{4.16}$$

The p-value is the probability that the resulting χ^2_{min} value or any bigger χ^2 value from the fit is achieved due to the statistical fluctuations of the measurements, when assuming that the underlying theory is correct [34]. The probability distribution function of χ^2 converges towards a normal distribution with a standard value of n and a standard deviation of

$\sqrt{2n}$ for large values of n. Thus, the p-value for the result $\chi^2/n = 1$ and big values of n converges towards 0.5, which corresponds to an optimal fit. [26]

The experimental values used in the following calculations are taken from [13]. The value for $A_{CP}(K^+\pi^0)$ has been changed following a new measurement reported by LHCb [35]. First, the measurements for $B \to K\pi$ are shown (Tab. 4.1), followed by the values for $B \to K^*\pi$ (Tab. 4.2).

	BR [10^{-6}]	A_{CP}	S_{CP}
$B^+ \to K^0\pi^+$	23.7 ± 0.8	-0.017 ± 0.016	
$B^+ \to K^+\pi^0$	12.9 ± 0.5	0.031 ± 0.013	
$B^0 \to K^+\pi^-$	19.6 ± 0.5	-0.083 ± 0.004	
$B^0 \to K^0\pi^0$	9.9 ± 0.5	0.00 ± 0.13	0.58 ± 0.17

Table 4.1: *Measured branching ratios, CP asymmetries for the $B \to K^*\pi$ decays and the mixing-induced CP asymmetry for for the $B \to K^0\pi^0$ decay [13] [35]*

	BR [10^{-6}]	A_{CP}
$B^+ \to K^{*0}\pi^+$	10.1 ± 0.8	-0.04 ± 0.09
$B^+ \to K^{*+}\pi^0$	6.8 ± 0.9	-0.39 ± 0.21
$B^0 \to K^{*+}\pi^-$	7.5 ± 0.4	-0.27 ± 0.04
$B^0 \to K^{*0}\pi^0$	3.3 ± 0.6	-0.15 ± 0.13

Table 4.2: *Measured branching ratios and CP asymmetries for the $B \to K\pi$ decays [13]*

The additional parameters in the calculations are not necessarily known precisely. Thus, it has to be accounted for the uncertainty of their values. For this reason, they have been introduced as nuisance parameters. They are Gaussian-constrained around their given value within their error, meaning that they contribute to the χ^2 value if they deviate from their initial estimate. The used nuisance parameters are the two angles of the CKM-matrix $\gamma = (71.1 \pm 5.3)°$ and $\beta = (22.2 \pm 0.7)°$ [13], the constant $R = 49.1 \pm 1.0$ in equation 4.12 [26] used in the approximation 4.11. Using the value for R, the prefactor of the approximation 4.11 $K \equiv \frac{3}{2}\frac{c_9}{c_1}R$ is -0.639 ± 0.013. Hence, the electroweak penguin diagram is approximated to have roughly two thirds of the strength of the tree diagram. The factor between the squared amplitude and the BR in equation 4.7 defined as $d^{(*)} \equiv \frac{\tau p}{8\pi m^2}$. In the following, d denotes the constants for the $B \to K\pi$ decays, while d^* denotes the values for $B \to K^*\pi$.

The constant $d^{(*)}$ has been calculated using the PDG values and their errors of the contributing constants for the different decays (see table 4.3).

	$d[10^{-12}eV^{-2}]$	$d^*[10^{-12}eV^{-2}]$
$B^+ \to K^{(*)0}\pi^+$	8246 ± 20	7539 ± 18
$B^+ \to K^{(*)+}\pi^0$	8261 ± 20	7554 ± 18
$B^0 \to K^{(*)+}\pi^-$	7653 ± 20	6997 ± 18
$B^0 \to K^{(*)0}\pi^0$	7654 ± 20	6999 ± 18

Table 4.3: *Decay constants for the calculation of the branching ratios from the decay amplitudes for all considered decays*

It can easily be seen in table 4.3 that the main differences in $d^{(*)}$ are between the B^+ and the B^0 decays. This difference comes from the different lifetimes of the two particles. The different masses of the decay products have a much smaller influence on the constants. These differences are far below 1%, which is small compared to the uncertainties of the approximation in equation 4.11 and the measurement errors. Therefore, calculating these constants exactly has no significant impact for the results, but reduces the number of uncertainty factors, which makes it easier to trace errors back.

4.2 Results

4.2.1 Fit up to second Order

Without making any approximation, the number of free parameters in equations 4.2 - 4.5 is larger than the number of values to fit to from tables 4.1 or 4.2. This means that the number of free parameters has to be reduced in order to achieve a meaningful result. As a first step, only the contributions of the first two orders will be considered. In addition with the approximation 4.11, the amplitudes, including their strengths and strong phases, are reduced to the following form.

$$A^{0+} = -P'_{tc} \tag{4.17}$$

$$\sqrt{2}A^{+0} = -T'e^{i\gamma} + P'_{tc} - \frac{3}{2}\frac{c_9}{c_1}RT' \tag{4.18}$$

$$A^{+-} = -T'e^{i\gamma} + P'_{tc} \tag{4.19}$$

$$\sqrt{2}A^{00} = -P'_{tc} - \frac{3}{2}\frac{c_9}{c_1}RT' \tag{4.20}$$

Since only one gluonic amplitude is left in this approximation, P'_{tc} is replaced by P' in the following. Now, the set of free parameters is reduced to the strength of the strong gluonic penguin amplitude $|P'|$, its strong phase $\delta_{P'}$, and the strength of the tree amplitude $|T'|$. Also, the calculated direct CP asymmetry in this approximation is zero for the decays $B^+ \to K^0\pi^+$ and $B^0 \to K^0\pi^0$ because both a strong and weak phase in the decay amplitude are needed for a CP violation to appear. Following equation 4.9, S_{CP} for the decay $B^0 \to K^0\pi^0$ has also no dependence on the parameters, since it only depends on the asymmetry in this decay, which cancels out here.

$B \to K\pi$:

Using the least squares method introduced above, the three free parameters ($|P'|$, $\delta_{P'}$ and $|T'|$) and the nuisance parameters can now be fit to the measurements leading to the result shown in table 4.4. Since the relative errors on the constant $d^{(*)}$ are very small, changes in these parameters of only a few percent have a strong impact on χ^2. Thus, the changes on these values in the minimization process are negligible. Because of that, these values are in general not shown.

$|P'|$ [eV]	$\delta_{P'}[°]$	$|T'|$ [eV]	$\gamma[°]$	R	$\frac{\chi^2}{d.o.f.}$	p-value
53.1 ± 0.5	-12.5 ± 0.7	9.1 ± 0.5	61 ± 3	49 ± 1	$65.7/3$	< 0.0001

Table 4.4: *Estimated theory and nuisance parameters from the fit up to second order on the $K\pi$ data*

As expected, the gluonic penguin amplitude $|P'|$ is estimated to be dominating, while the tree amplitude has a magnitude of less than 20% compared to $|P'|$. The goodness of fit value $\frac{\chi^2}{d.o.f.} = 65.7/3$ as well as the p-value of < 0.0001 indicate large discrepancies between the model and the data. The uncertainties on the parameters have been calculated as explained in section 4.1.5. Since only one parameter is varied here, these uncertainties give information on the impact of the parameter on the χ^2 value. Thus, they cannot be directly interpreted as error bounds for the actual amplitude or phase strengths. This is valid for all following parameter errors.

This result can also be visualized as follows. Since the amplitude is squared in the BR calculation, the strong phase $\delta_{P'}$ cancels out in the calculation of $\mathrm{BR}(K^0\pi^+)$. Thus, $|P'|$ is the only sizable parameter contributing to the amplitude of the $B^+ \to K^0\pi^+$ decay, so this parameter is estimated most precisely. This is reflected by the estimated error on $|P'|$ in table 4.4. In order to look at the further parameters $|T'|$ and $\delta_{P'}$, $|P'|$ has been set constant in the following representation. Then, a scan in the parameter plane of $|T'|$ and $\delta_{P'}$ has been performed marking each point which is within $\pm 1\sigma$ from the corresponding measurement. This gives "allowed" regions for all measurements in the $|T'|$-$\delta_{P'}$ plane.

Since $|P'|$ is taken to be constant this visualization has only qualitative value. The result is shown in figure 4.3.
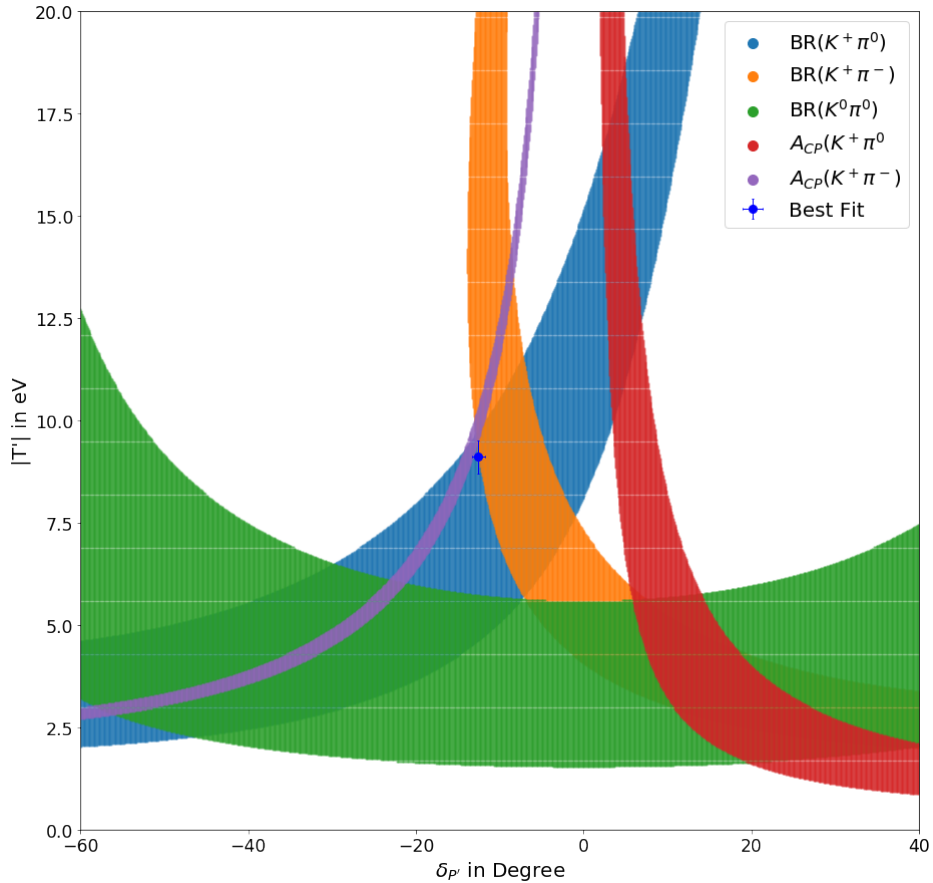
Figure 4.3: *Visualization of the fit up to second order on the $K\pi$ data in the $|T'|$-$\delta_{P'}$ plane*

Figure 4.3 clearly shows that the maximum likelihood estimation is dominated by the precise measurement on A_{CP}^{+-} displayed in purple. In this approximation no fit point can be found which matches all measurements to a reasonable degree. There is no single point in which all allowed regions overlap but rather several regions of partial agreement. Especially the measurements $A_{CP}(K^+\pi^0)$ (red) and $\mathrm{BR}(K^0\pi^0)$ (green) do not match the fit point. By plugging the estimated values back into the equations, these discrepancies can be calculated. The theoretical value for $\mathrm{BR}(K^0\pi^0)$ using $\hat{\vec{\theta}}$ is 8.8×10^{-6}, which is more than 2σ away from the measurement of $(9.9 \pm 0.5) \times 10^{-6}$. As expected, this approximation fails to reproduce the different signs of the two significant A_{CP} measurements $A_{CP}(K^+\pi^0)$ and $A_{CP}(K^+\pi^-)$, which is the core of the $K\pi$-puzzle. The theoretical value for $A_{CP}(K^+\pi^0)$ in

this approximation is -0.065 compared to the measurement of 0.037 ± 0.021. In addition, this fit has been reached by forcing the weak phase γ to $61 \pm 3°$, significantly below the measured value of $\gamma = (71.1 \pm 5.3)°$.

$B \to K^*\pi$:

Performing the same fit on the data for the $B \to K^*\pi$ decays yields the following results (table 4.5).

$|P'|$ [eV]	$\delta_P[°]$	$|T'|$ [eV]	$\gamma[°]$	R	$\frac{\chi^2}{d.o.f.}$	p-value
34.2 ± 0.8	-17 ± 3	13 ± 2	61 ± 3	49 ± 1	$12.2/3$	0.0067

Table 4.5: *Estimated theory and nuisance parameters from the fit up to second order on the $K^*\pi$ data*

Once again, the prediction that the gluonic penguin amplitude dominates is met. Due to the larger errors, the $\frac{\chi^2}{d.o.f.}$ value of $12.2/3$ is lower than in the previous case. The p-value of 0.0067 still indicates a bad fit. Performing the same qualitative visualization as before leads to figure 4.4.

Again, the precise measurement for A_{CP}^{+-} has a large effect on the optimal fit values $\hat{\vec{\theta}}$. Here, the discrepancy between the two A_{CP} measurements does not exist. This is a result from the fact that both measurements have the same sign here as shown in 4.2. Analogously, the approximation to the second order fails to fit to the measurement on $\mathrm{BR}(K^{*0}\pi^0)$ and reduces the weak phase γ below the target value.

4.2.2 Impact of C'

In order to resolve the flaws of the current approximation, an additional component of third order shall be introduced. The color suppressed tree amplitude is likely to be the biggest one of this order and could potentially resolve the $K\pi$-puzzle [36]. Due to the different final states of the decays $B^+ \to K^+\pi^0$ and $B^0 \to K^+\pi^-$, the color suppressed tree diagram only appears in the $B^+ \to K^+\pi^0$ decay. This diagram has in general a different strong and weak phase than the leading amplitude P'. This results in a contribution to the direct CP asymmetry, which does not appear in the $B^0 \to K^+\pi^-$ decay. The interaction of the color suppressed (C') and allowed tree diagram (T') leads to no term in the direct CP asymmetry, because they have the same weak phase. In order to test the effect of the color suppressed tree amplitude C', it has been introduced at varying strengths to see weather this amplitude can resolve the discrepancy, and if so at what strength. While the magnitude of this decay diagram was fixed, the other parameters including the strong phase of this amplitude $\delta_{C'}$ could float freely to find the best fitting point in the parameter space. In the following figure, the best fitting values for the important asymmetries in $K\pi$
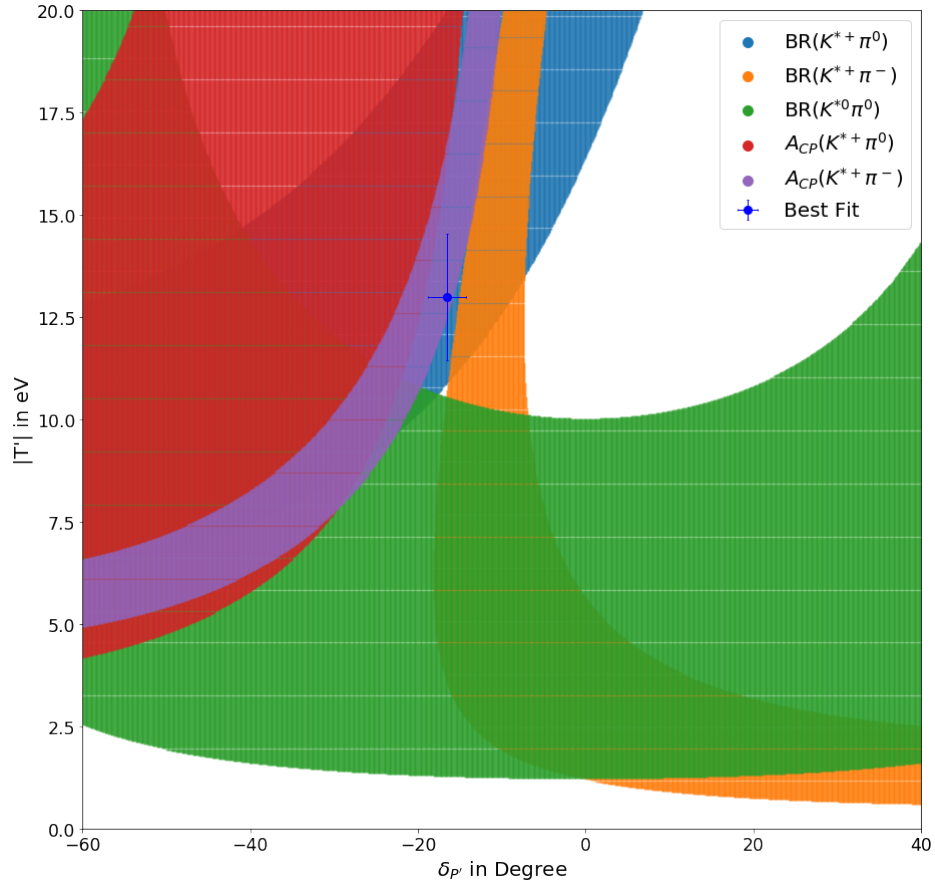
Figure 4.4: *Visualization of the fit up to second order on the $K^*\pi$ data in the $T^{'}$-δ_P plane*

are plotted in dependence on the strength of $|C'|$ (figure 4.5 a). By introducing the color suppressed tree diagram the asymmetry $A_{CP}(K^0\pi^0)$ does not vanish in the approximation any more. Due to the large error on this measurement, this constraint is met for all cases and is thus not displayed in figure 4.5 a). Nonetheless, the three non-zero asymmetry values and the resulting asymmetry sum rule parameter from equation 4.10 in dependence of $|C'|$ can now be plotted (figure 4.5 b).

In figure 4.5 a), the dotted lines are the current measurements of the asymmetries which are surrounded by areas with matching color. These areas represent the current $\pm 1\sigma$ errors. The lines are the fit result after the optimization. The result is consistent with the fit up to the second Order. Without C', the different signs of the direct asymmetries $A_{CP}(K^+\pi^0)$ and $A_{CP}(K^+\pi^-)$ can not be explained. But with the introduction of the additional amplitude C', the this can be solved even for small contributions of C' (see figure 4.5 a). Hence, the $K\pi$-puzzle can be solved by using the SM amplitudes, which makes NP effects unlikely.
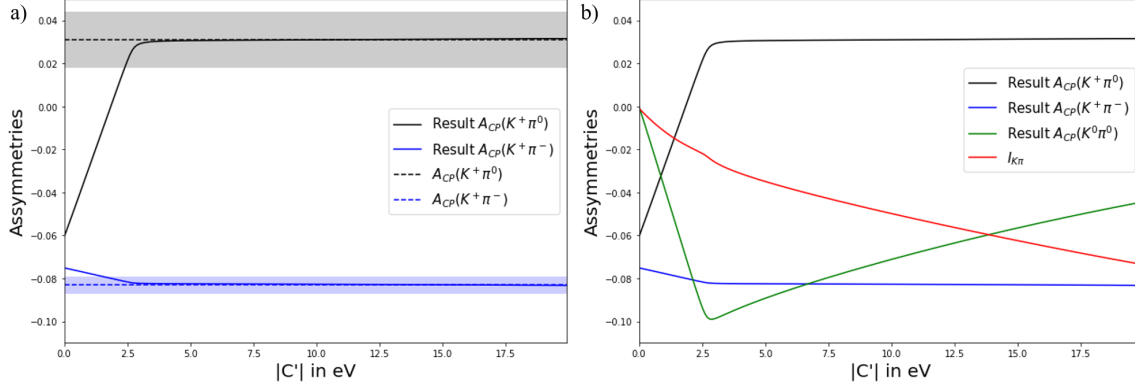
Figure 4.5: *Adjustment of the key asymmetries (a) and behavior of all non zero asymmetries and the resulting $I_{K\pi}$ value (b) in dependence on the strength of the color suppressed tree diagram C' for $K\pi$*

Figure 4.5 b) shows that the calculated A_{CP} values are not consistent with a small value for $I_{K\pi}$ for increasing values of $|C'|$. As the asymmetries adjust, the magnitude of $I_{K\pi}$ increases with $|C'|$. Hence, $|C'|$ is chosen in a way that the measurements can be explained, but $I_{K\pi}$ is still relatively small. Following this reasoning, $|C'|$ will be introduced using the naive color suppression factor of $1/3$ as $|C'| = |T'|/3$ for the $B \to K\pi$ decays.

A figure corresponding to 4.4 for the $B \to K^*\pi$ does not show such clear error sources. Still, the fit value of $\frac{\chi^2}{d.o.f.} = 12.2/3$ can be improved. To do so, the color suppressed tree amplitude is introduced as a free parameter here.

4.2.3 Introduction of C'

After introducing the color suppressed tree amplitude the new model can be fit to the data again using the following equations.

$$A^{0+} = -P'_{tc} \tag{4.21}$$

$$\sqrt{2}A^{+0} = -T'e^{i\gamma} - C'e^{i\gamma} + P'_{tc} - \frac{3}{2}\frac{c_9}{c_1}RT' \tag{4.22}$$

$$A^{+-} = -T'e^{i\gamma} + P'_{tc} \tag{4.23}$$

$$\sqrt{2}A^{00} = -C'e^{i\gamma} - P'_{tc} - \frac{3}{2}\frac{c_9}{c_1}RT' \tag{4.24}$$

By using the relation 4.11 analogously for C' and $P_{EW}^{'C}$, the color suppressed electroweak penguin amplitude could be introduced into the calculation without adding a new free parameter [26]. The uncertainty here would be the same as in 4.11. Nevertheless, the prefactor in 4.11 suggests that the strength $|P_{EW}^{'C}|$ is below 5% of the leading diagram $|P'|$. Contributions of that size are not considered, since they are small compared to the uncertainties in the measurements and are not needed to explain the different sign in the A_{CP} measurements of the $B \to K\pi$ decays. Thus, they are not expected to have significant impact on the allowed regions in the parameter plane and the parameter estimation. To test this, parameter estimations with $P_{EW}^{'C}$ and with all contributions have been performed. As expected, these fits give qualitatively similar results, as the overlay of the allowed regions cover the same parameter values. In addition to that, the same measurements are inconsistent with the best fit point.

$B \to K\pi$:

For the $B \to K\pi$ decays with a free strong phase $\delta_{C'}$ and a magnitude of $|C'|$, which is fixed to $|C'| = |T'|/3$ the fit yields the set of results displayed below.

$|P'|$ [eV]	$\delta_{P'}[°]$	$|T'|$ [eV]	$\delta_{C'}[°]$	$\gamma[°]$
53.5 ± 0.5	-9.3 ± 0.5	13.0 ± 0.6	-47 ± 6	64 ± 3
$\beta[°]$	R	$\frac{\chi^2}{d.o.f.}$	p-value	
22.2 ± 0.7	49 ± 1	$5.6/4$	0.2311	

Table 4.6: *Estimated theory and nuisance parameters from the fit up on the $K\pi$ data after introducing $|C'| = \frac{|T'|}{3}$*

Since A_{CP}^{00} is not zero in this approximation, the constraint on S_{CP} from equation 4.9 can be used here as well. This enables an estimation of β next to the new phase $\delta_{C'}$. The new estimated parameters show the same strength structure as before. The estimated magnitude for the new amplitude can be calculated from the strength of the color allowed tree diagram and is $\frac{|T'|}{3} = |C'| = (4.3 \pm 0.2)$eV. Due to this small magnitude, the strong phase can not be determined precisely compared to the strong phase $\delta_{P'}$ in this approximation. The estimate for the weak phase γ increased and fits better to the current measurement now. Overall, the fit improved to a goodness-of-fit value of $\frac{\chi^2}{d.o.f.} = 5.6/4$. This corresponds to the p-value 0.2311. Using the fit parameters, the prediction for $I_{K\pi}$ is -0.033.

Figure 4.6 shows these results. As intended, the measured asymmetries can be explained now within the error margins and thus overlay in the representation. Due to the imprecise measurement on A_{CP}^{00}, this contribution and the correlated S_{CP} impose weak constraints
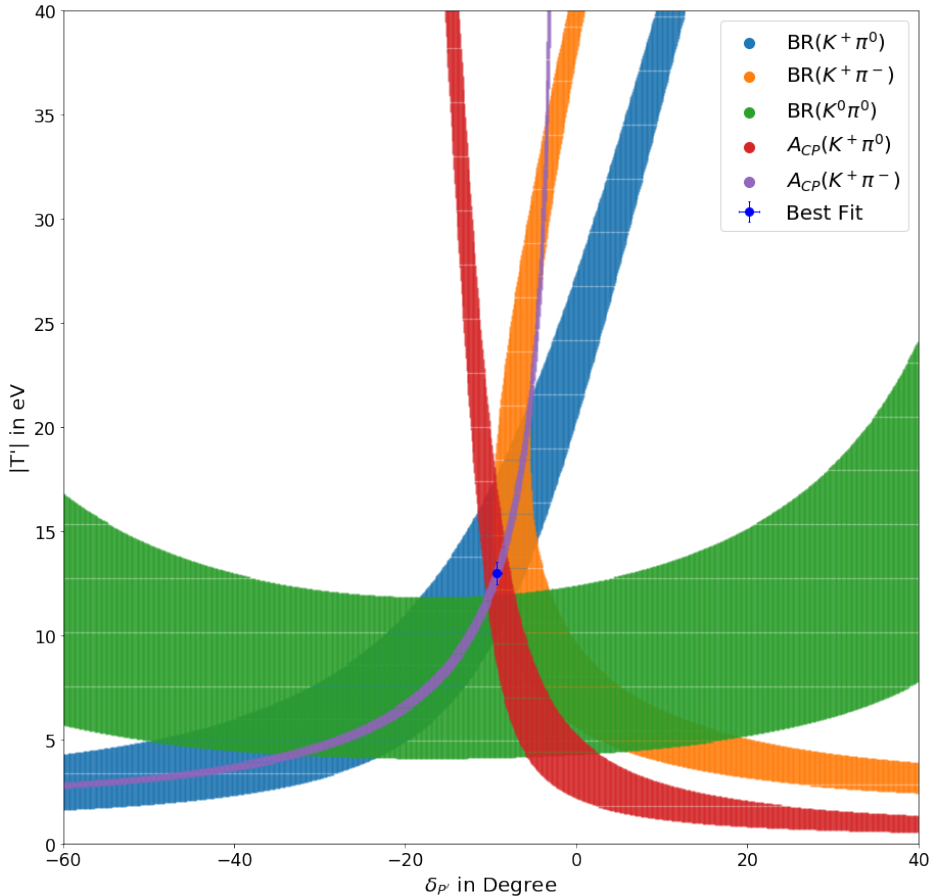
Figure 4.6: *Visualization of the fit result on the $K\pi$ data after introducing $|C'| = \frac{|T'|}{3}$ in the $|T'|$-$\delta_{P'}$ plane*

on the free parameters. The allowed regions here cover the complete displayed parameter space. For this reason, they are not shown in figure 4.6 even though they have been used in the calculations. Using the best fit parameters $\hat{\vec{\theta}}$, the asymmetry prediction is $A_{CP}^{00} = -0.09$, which is well within the 1σ region of the measured value.

With the introduction of $\delta_{C'}$, this result could also be displayed in different parameter planes including $\delta_{C'}$. Due to the small impact of $\delta_{C'}$, the allowed regions in this representation become large and the resulting plot gives no additional information. For this reason, they will not be shown here.

As can be seen in figure 4.6, most measurements constrain the parameter space mainly in $\delta_{P'}$ in the best fit region, while the strength of the color allowed tree diagram T' is only weakly bound. This follows from the vertical orientation of the corresponding

bands in the representation. The only measurement which imposes a stronger bound on $|T'|$ than on $\delta_{P'}$ due to its horizontal orientation is the value for $BR(K^0\pi^0)$, which is displayed in green. Unfortunately, this measurement still has a comparably large error. Experimentally this channel is difficult to measure, since this all-neutral final state is difficult to measure. Hence, this decay has the potential to improve the parameter estimation and ultimately the understanding of the $B \to K\pi$ system. The possible impact of a more precise measurement of Belle II on $BR(K^0\pi^0)$ (a) compared to $BR(K^+\pi^0)$ (b) is shown in figure 4.7.
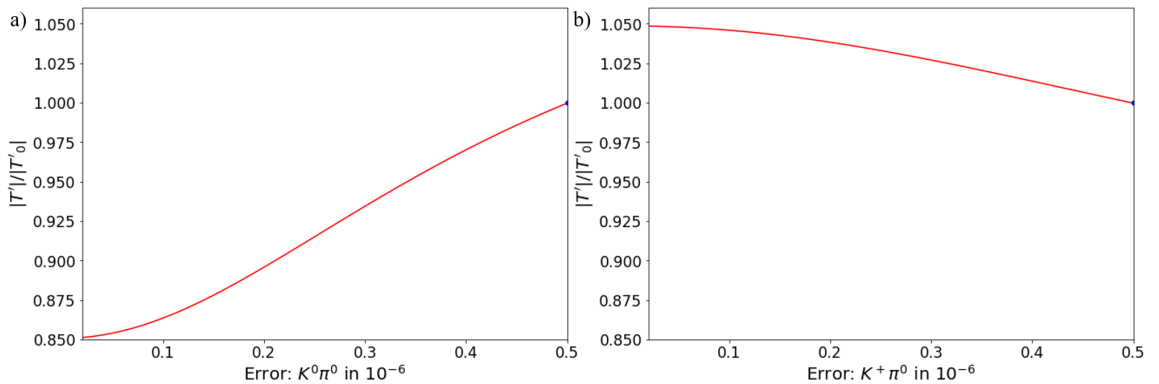
Figure 4.7: *Analysis of the impact of decreasing measurement errors on the estimate for $|T'|$ compared to the current estimate*

Here, it is shown how the value of $|T'|$ changes if certain measurement values stay the same but get more precise. As expected, $B^0 \to K^0\pi^0$ has a larger potential impact on $|T'|$. For an error close to zero on this measurement, the magnitude of T' changes by roughly 15%, while the same error reduction on $B^+ \to K^+\pi^0$ leads to a change of almost 5% in this approximation.

In addition, the current best values can change with new more precise measurements, for example from Belle II. The $B^0 \to K^0\pi^0$ decay not only has the largest relative error on the BR measurement, but also imposes the largest discrepancy between the fit and the measurements. By looking at equation 4.24 it is clear that for larger values of $|T'|$ to be consistent with the BR of $B^0 \to K^0\pi^0$, the measured value is expected to decrease. The best fit is achieved at a value of 9.3×10^{-6}.

$B \to K^*\pi$:

Performing the fit with a free C' on the data for $B \to K^*\pi$ yields the results shown in table 4.7 and figure 4.8.

$\|P'\|$ [eV]	$\delta_P[°]$	$\|T'\|$ [eV]	$\|C'\|$ [eV]	$\delta_{C'}[°]$
34.6 ± 0.8	-13 ± 2	15 ± 2	10 ± 19	-1 ± 13
$\gamma[°]$	R	$\frac{\chi^2}{d.o.f.}$	p-value	
60 ± 3	49 ± 1	$14.1/2$	0.0009	

Table 4.7: *Estimated theory and nuisance parameters from the fit up on the $K^*\pi$ data after introducing C'*
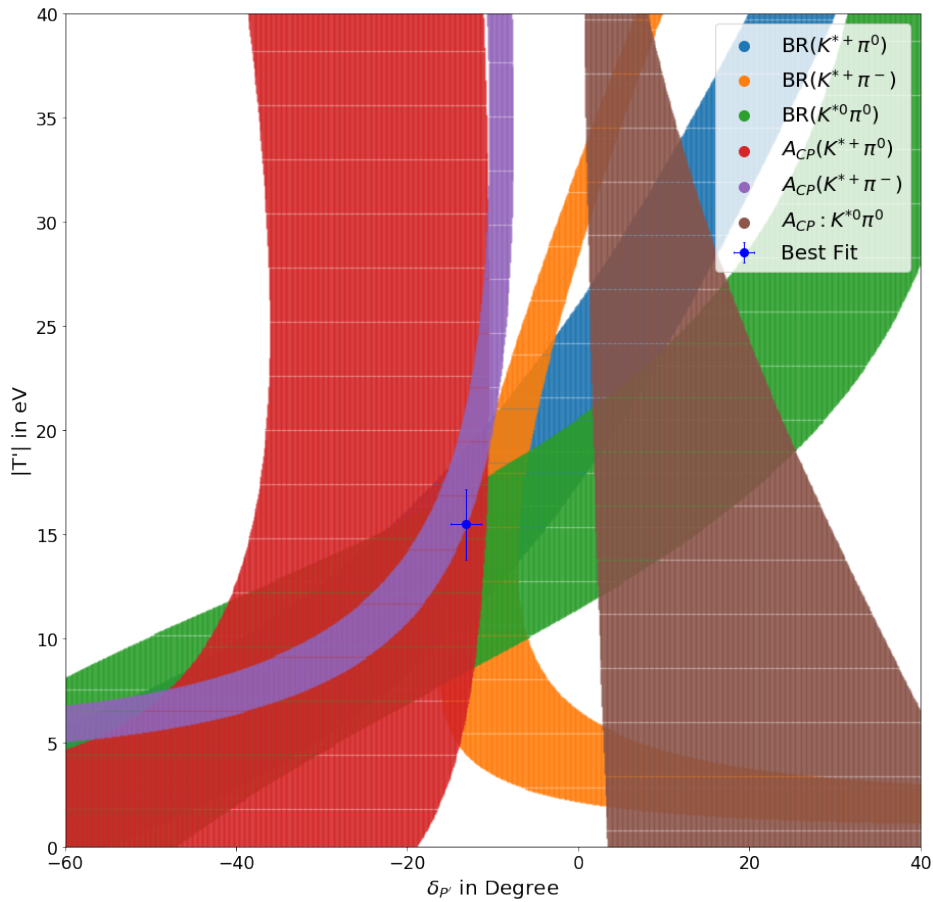
Figure 4.8: *Visualization of the fit result on the $K^*\pi$ data after introducing C' in the T'-δ_P plane*

In this case, the measurement on $A_{CP}(K^{*0}\pi^0)$ imposes an additional constraint on the parameters, which is plotted in brown in figure 4.8. With a goodness-of-fit value $\frac{\chi^2}{d.o.f.} = 14.1/2$ there is no improvement of the fit by introducing C'. The model is still

unable to reproduce the measured data. This lacking impact of the color suppressed tree diagram is also reflected in the large errors on both the estimated magnitude $|C'|$ and strong phase $\delta_{C'}$ of this amplitude. A possible explanation is that the problem of the different sign of A_{CP}^{+0} and A_{CP}^{+-} does not exist in this case. Also, the measurement A_{CP}^{00}, which can only be fitted with C', can not be met within 2σ. The calculated asymmetry from $\hat{\bar{\theta}}$ is 0.14 compared to the measurement of -0.15 ± 0.13. In addition, the weak phase γ has been lowered again by the estimate, which contradicts with the measurement. Due to the large uncertainties on the current measurements and the unsuccessful attempt to improve the fit, the $B \to K^*\pi$ decay parameters will not be further analyzed here. However, this puzzling behaviour in the $K^*\pi$ system could be a hint towards NP. Possible explanations within the SM can only be found by regarding the missing decay diagrams and potentially by treating P'_{EW} individually. In order to be able to determine the strengths of the decay diagrams for these decays and investigate these tensions, more precise measurements, which Belle II will deliver, are needed.

4.2.4 Introduction of $B \to \pi^+\pi^0$

Now, the parameter estimation for the $B \to K\pi$ shall be further improved. Due to the imprecise measurement on $B^0 \to K^0\pi^0$ and the discussed orientation of the bands representing the other measurements, $|T'|$ is not strongly constrained. In order to improve this, the measurement on $B \to \pi^+\pi^0$ can be introduced, which imposes such a constraint [37]. Following Fleischer et al. [37], the amplitude of this decay is related to the two tree diagrams by

$$|T' + C'| = R_{T+C} \left| \frac{V_{us}}{V_{ud}} \right| \sqrt{2} |A(B \to \pi^+\pi^0)|. \tag{4.25}$$

The ratio of the CKM matrix elements in equation 4.25 accounts for the fact that the strange quark in the kaon is replaced by a down quark to form the second pion in this decay. This fraction is introduced as a nuisance parameter with $\left| \frac{V_{us}}{V_{ud}} \right| = 4.34 \pm 0.09$. R_{T+C} is a SU(3) breaking factor with the value 1.2 ± 0.2, which has also been introduced as a nuisance parameter. In addition to that, the constant relating the squared amplitude with the BR has been calculated to be $d = (8890 \pm 22) \times 10^{-12}$eV. Relation 4.25 has the advantage that it only depends on the two tree amplitudes. Thus, it only imposes a constraint on $|T'|$ in the considered parameter plane with the constraint $|C'| = \frac{|T'|}{3}$. The measured BR of this decay is $(5.5 \pm 0.4) \times 10^{-6}$ [13]. Introducing this constraint to the fit gives the result shown in table 4.9.

Figure 4.9 clearly shows the constraint (brown vertical band in figure 4.9) of the $B \to \pi^+\pi^0$ decay on $|T'|$. However, there is a tension between the new input and the old result. The $\chi^2/d.o.f.$ value increased to 8.9/5, which is also considering the p-value of 0.1131 not a good fit, but cannot be rejected. As a result, the fitted value for T' decreased to (10.3 ± 0.3)eV, which determines $|C'|$ as (3.4 ± 0.1)eV. Using the best parameter set $\hat{\bar{\theta}}$ from

$|P'|$ [eV]	$\delta_P[°]$	$|T'|$ [eV]	$\delta_{C'}[°]$	$\gamma[°]$	$\beta[°]$
53.2 ± 0.5	-11.9 ± 0.6	10.3 ± 0.3	-128 ± 6	63 ± 3	22.2 ± 0.7
R	R_{T+C}	$\left|\frac{V_{us}}{V_{ud}}\right|$	$\frac{\chi^2}{d.o.f.}$	p-value	
49 ± 1	1.07 ± 0.05	4.35 ± 0.08	$8.9/5$	0.1131	

Table 4.8: *Estimated theory and nuisance parameters from the fit up on the $K\pi$ data after introducing $|C'| = \frac{|T'|}{3}$ and the measurement on $B \to \pi^+\pi^0$*
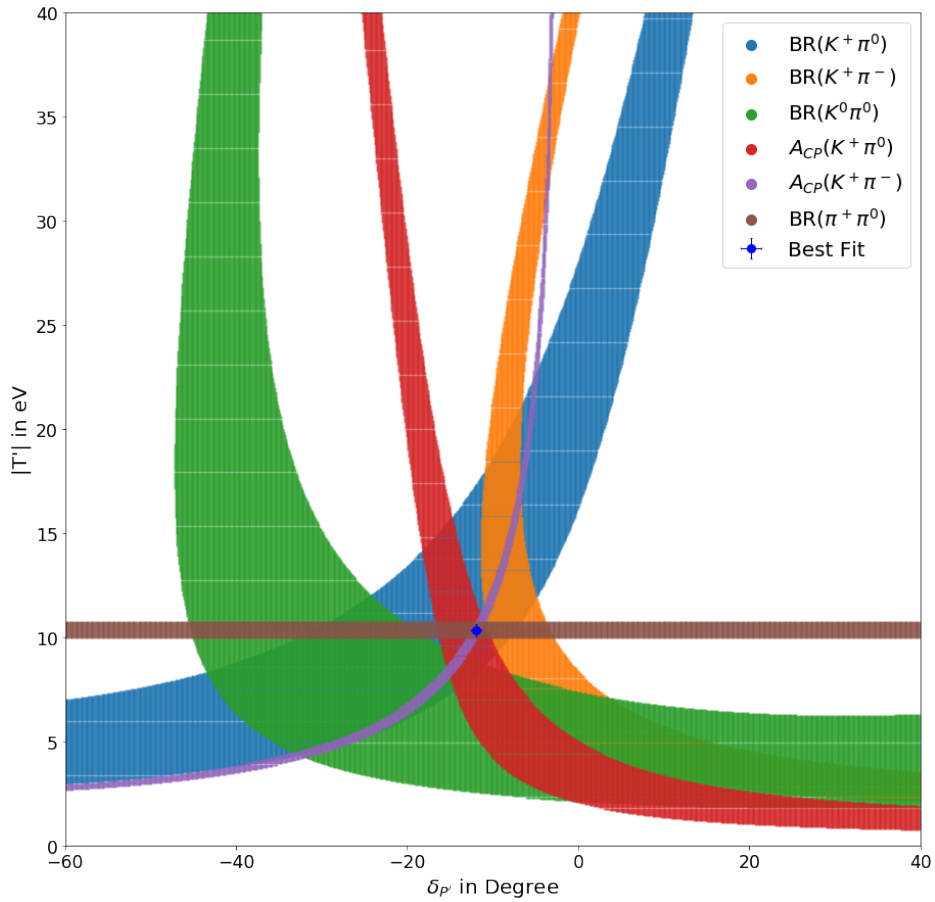
Figure 4.9: *Visualization of the fit result on the $K\pi$ data after introducing $|C'| = \frac{|T'|}{3}$ and the measurement on $B \to \pi^+\pi^0$ in the $|T'|$-$\delta_{P'}$ plane*

the estimation without the $B \to \pi^+\pi^0$ measurement a theoretical BR of 15.4×10^{-6} can be calculated for $B \to \pi^+\pi^0$. This strongly contradicts with the actual measurement of

$(5.5 \pm 0.4) \times 10^{-6}$ and shows the uncertainties of the quantitative values in the parameter estimation. This tension is resolved by a change in $\delta_{C'}$ to $(-128 \pm 6)°$. The prediction of $\hat{\bar{\theta}}$ for A_{CP}^{00}, which is not shown in figure 4.9 due to its large errors, can be calculated as -0.12. This is still within the error bounds of this measurement.

In order to resolve these tensions, the constraint on the magnitude of $|C'| = |T'|/3$ can be removed. In this case, the results of the fit are

$|P'|$ [eV]	$\delta_P[°]$	$|T'|$ [eV]	$|C'|$ [eV]	$\delta_{C'}[°]$	$\gamma[°]$
53.2 ± 0.5	-11.7 ± 0.6	10.5 ± 0.3	2.8 ± 0.4	-102 ± 8	64 ± 3
$\beta[°]$	R	R_{T+C}	$\left|\frac{V_{us}}{V_{ud}}\right|$	$\frac{\chi^2}{d.o.f.}$	p-value
22.2 ± 0.7	49 ± 1	1.26 ± 0.05	4.34 ± 0.08	$7.7/4$	0.1032

Table 4.9: *Estimated theory and nuisance parameters from the fit up on the $K\pi$ data after introducing C' with a free floating magnitude and strong phase and the measurement on $B \to \pi^+\pi^0$*

With the new p-value of 0.1032, the fit worsened compared to before. Even though the alignment of the bands seen in figure 4.10 and therefore the predictions for the measurements improved, the decreased number of degrees of freedom lets the fit quality decrease overall. Again, $B^0 \to K^0\pi^0$ is slightly off (green band in figure 4.10), which highlights the importance of this measurement. The best fit relation between the color-suppressed and -allowed amplitude strengths is close to the naive assumption of $\frac{1}{3}$. This supports the assumption made above. Still, the value of $\delta_{C'}$ changed by more that 1σ compared to the previous fit, indicating that the strong phase of C' has a high potential to resolve tensions in the measurements. This big parameter change is possible, since this value is not strongly bound by any measurement, like e.g. $|P|$ is from $BR(K^0\pi^+)$.

4.2.5 Summary

In summary, for $B \to K\pi$ the measured values for the branching ratios and direct CP asymmetries could be fitted with $\frac{\chi^2}{d.o.f.} = 5.6/4$ after introducing the color suppressed tree diagram to the approximation up to the second order. By doing this, the different signs of A_{CP}^{+0} and A_{CP}^{+-} could be explained within the SM. Still, tensions coming mainly from the measurements on $B^0 \to K^0\pi^0$ and also $B^+ \to \pi^+\pi^0$ persist. Here, more precise measurements from Belle II are needed, which could then lead to the necessity of introducing NP. However, since the introduction of the color suppressed tree diagram could resolve the $K\pi$-puzzle the discovery of NP, which is expected in the P' diagrams, is unlikely.

The $B \to K^*\pi$ system could be fitted with a quality of $\frac{\chi^2}{d.o.f.} = 12.2/3$ in the approximation to the second order. Introducing C' failed to improve the fit. The large relative errors on
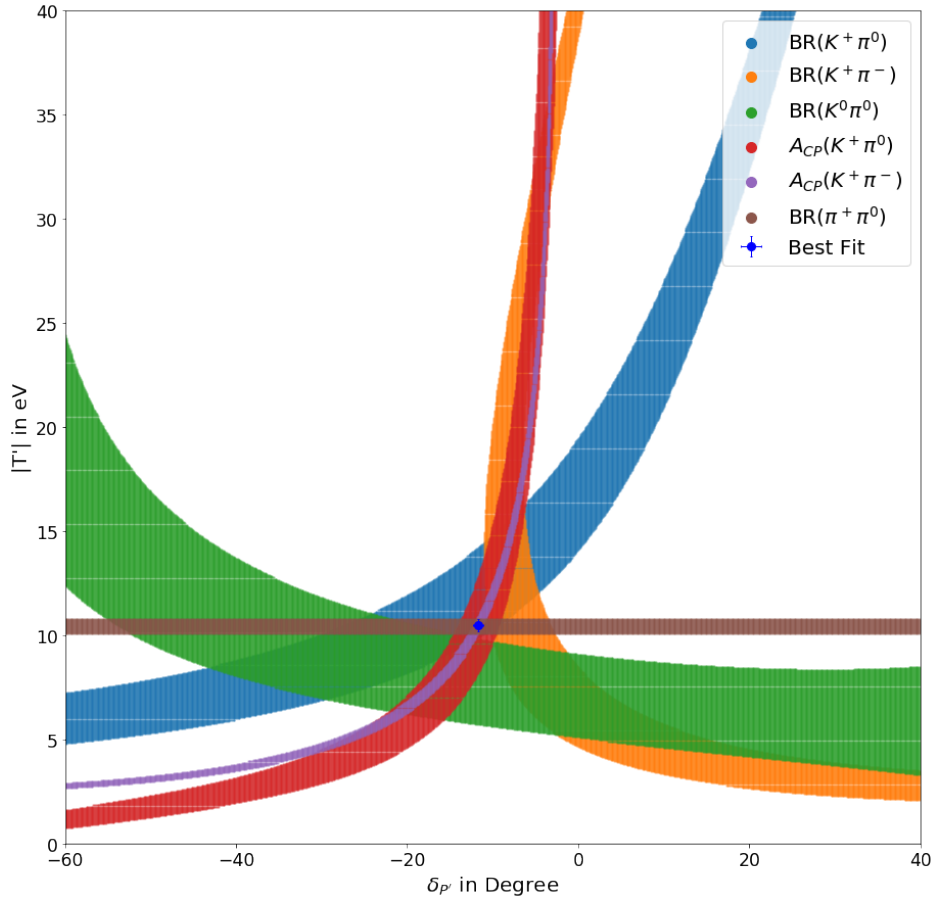
Figure 4.10: *Visualization of the fit result on the $K\pi$ data after introducing C' with a free floating magnitude and strong phase and the measurement on $B \to \pi^+\pi^0$ in the $|T'|$-$\delta_{P'}$ plane*

these measurements hinder a more sophisticated analysis. More precise data is needed in order to extract theory parameters with a better precision or to potentially reject the SM as an explanation.

5 Analysis of $B^+ \to K^*(892)^+[K_S^0\pi^+]\pi^0$

With the larger instantaneous luminosity at Belle II and the refined detection and analysis tools, this experiment facilitates more precise measurements. In the following section, the ongoing analysis on the decay channel $B^+ \to K^*(892)^+[K_S^0\pi^+]\pi^0$ is presented[1]. This includes, if not differently stated, the charge conjugated channel. As discussed above, a precise measurement of the branching ratio (BR) and direct CP violation of this decay channel can provide stringent tests of the SM and even require extensions of the present particle physics theories. This channel has been chosen, since it is currently measured with the highest direct CP violation in the $B \to K^*\pi$ system, but still has large uncertainties. In addition, this channel is hard to measure for the LHC due to the π^0 in the final state.

5.1 Blind Analysis

In general, all Belle II analyses are performed in a "blind" mode. This means that the analysis on the individual channels is performed and optimized exclusively on simulated data. After the quality of the analysis is validated, it can be unblinded. In the unblinding process, the analysis is performed on the actual data from the experiment. After the unblinding, the analysis must not be changed any more. This procedure is used to make sure that it is not possible to willingly or unwillingly bias the results of the measurement by tuning the analysis method and tools.

This analysis is still in the development stage and the data used to this point are solely simulated Monte Carlo (MC) events. A data set of 700fb^{-1} generic MC data on the $\Upsilon(4S)$ resonance is used. Generic MC includes $B^0\bar{B}^0$, B^+B^-, $u\bar{u}$, $d\bar{d}$, $c\bar{c}$ and $s\bar{s}$ events in the correct proportions [38]. This data set is comparable to the total data accumulated by the Belle experiment but small compared to the aimed integrated luminosity of Belle II of 50ab^{-1} by the middle of this decade. In addition, a simulated data set of 2×10^6 signal events for $B^+ \to K^*(892)^+[K_S^0\pi^+]\pi^0$ has been produced to study the characteristics of this decay in the detector in detail.

---

[1]The presented work has been achieved in a joint effort with Markus Reif.

5.2 Event Selection

As displayed in table 4.2 the current BR measurement as given by the Particle Data Group (PDG) for the decay $B^+ \to K^*(892)^+\pi^0$ is $(6.8\pm0.9)\times10^{-6}$. The $K^*(892)^+$ almost exclusively decays into $K^+\pi^0$ and $K^0_S\pi^+$ [13]. A sophisticated event selection is needed in order to distinguish the signal events from the generic data. To do so, the event variables, which are generated from the detector data, are analyzed. The allowed event variable ranges can be narrowed down to intervals which fit to the considered decay. All events in which a certain variable is outside the allowed range are excluded from the analysis. This is called performing cuts on the data set. In the first skims, loose cuts are performed with the aim to keep almost all signal events but reject enough background to get a considerably smaller data set. On this data set, more sophisticated selection criteria will be applied.

5.2.1 Reconstruction

As a first step, loose cuts on the final state particle candidates are applied. These candidates can then be combined in a kinematic fit obeying the decay topologies to reconstruct B meson candidates. The used first selections follow the general selection criteria of the Belle II charmless working group.

For the charged pion candidates, it is required for the track to be in the acceptance region of the CDC. Then, a fit can be performed on this track in the CDC. Only candidates with a positive p-value are retained. In addition, loose cuts are applied on the impact parameter of the charged pion. The origin of the particle as determined by the track fit is required to have an absolute radial distance of $|dr| < 0.5$cm and a distance along the beam pipe of $|dz| < 3$cm to the IP. These cuts help to especially reject events produced from cosmic radiation or interactions of the beam with residual gas in the beam pipe.

The final state π^0 particles decay with a probability of $(99.823 \pm 0.034)\%$ into two photons [13]. These photons are reconstructed from clusters in the ECL. The individual photons are required to have an energy above 22.5MeV if they are reconstructed in the forward end cap region and an energy above 20MeV if they are reconstructed in the barrel or backward end cap region of the ECL. The combined mass of the two photons forming a π^0 is restricted to the range $105 < m(\gamma\gamma) < 150$MeV. Also, a mass fit on the two photons is performed. Only candidates in which the fit converged are kept.

The K^0_S decays with a probability of $(30.69 \pm 0.05)\%$ into $\pi^0\pi^0$ and with $(69.20 \pm 0.05)\%$ into $\pi^+\pi^-$ [13]. Here, the neutral kaon is only reconstructed from the $\pi^+\pi^-$ decay channel. Hence, the later result has to be rescaled accordingly. The reconstructed mass is required to be in the window of $450 < m(K^0_S) < 550$MeV and the vertex fit for the kaon has to

converge. In order to reduce combinatorial background, additional constraints are applied on variables describing the kinematics of the K_S^0. These are the momentum and flight distance of the K_S^0. In addition, the distance between the trajectories of the two charged pion candidates and the angle between the K_S^0 flight direction and the two pion pair momentum are restrained. [38]

From the charged and neutral particles passing the above cuts, the full decay chain can be reconstructed following the decay topology. First, the $K^*(892)^+$ is formed from a π^+ and a K_S^0. The resulting mass is restricted to $0.7 < m_{inv}(K^*(892)^+) < 1.6\text{GeV}$. Finally, this $K^*(892)^+$ candidate can be combined with a π^0 candidate to form a B^+ meson candidate. Now, full event variables can be investigated. The beam constrained mass M_{bc} is given by

$$M_{bc} = \sqrt{E_{beam}^2/c^4 - p_B^2/c^2},$$

(5.1)

[39] where E_{beam} is half of the center-of-mass energy of the collision and p_B is the three-momentum of the B^+ meson candidate in this frame. The variable M_{bc} has a natural upper limit, since it must be smaller or equal to the half of the center-of-mass energy of the collision. At the $\Upsilon(4S)$ resonance, the upper limit is approximately 5.29GeV. Since the $\Upsilon(4S)$ has just enough mass to produce a B meson pair, this upper limit can be reached. All candidates above that value are not physical and are rejected. The first loose cut range here is $5.2 < M_{bc} < 5.29\text{GeV}$. In addition,

$$\Delta E = E_{reco} - E_{beam}$$

(5.2)

can be calculated, where E_{reco} denotes the reconstructed energy of the B meson in the center-of-mass system. Note that E_{reco} is calculated from the individual 4-vectors in the decay particles of the B meson. ΔE is in theory centered around 0. The first skimming cut on this variable is set as $|\Delta E| < 0.5\text{GeV}$.

5.2.2 Misidentification

In the reconstruction process, several mistakes can appear. For instance, a signal event can be misreconstructed as a background event if a particle in the decay chain is misidentified. In this case, the mass hypothesis of the misidentified particle is wrong, which also results in a flawed mass reconstruction of the intermediate decay particles. This error can also happen inverse if a background event is misreconstructed as signal. This can not only happen due to a particle hypothesis mistake but also by using particles in the decay chain which actually come from the other B meson and randomly fulfill the selection criteria.

5.2.3 Optimization of the Signal Selection

Due to imperfect reconstruction of the decay particles and the possible wrong particle combinations, the measured event variables of the signal cover a certain range. Hence, performing cuts can not only exclude background events but also signal events. The aim of the ongoing selection is to most efficiently exclude background and maintain signal events. One approach here is to maximize the Figure of Merit (FOM), which is given by

$$FOM = \frac{S}{\sqrt{S+B}} \qquad (5.3)$$

[40]. Here, S and B are the number of signal and background events respectively, which survive a certain cut. By choosing the cut which maximizes the FOM, the statistical significance of the remaining signal events in the resulting data set is maximized. An optimization can be made in the π^0 reconstruction. Combinatorial background can result from soft photons, which are collinear with the π^0. This background shall be rejected by the FOM optimized cut $|cosHelicityAngleMomentum| < 0.96$. This variable returns the cosine of the angle between the two photon momentum difference (a momentum 3-vector $\Delta \vec{p_{\gamma\gamma}}$) in the π^0 rest frame and the π^0 momentum in the lab frame.

However, if the background in a certain variable can be simulated it can also be beneficial to apply looser cuts. This analysis aims for a 2D fit of the simulated data in the variables ΔE and M_{bc}. The background shapes will be extracted and fit to in these variables. Hence, they are not FOM optimized to allow for a better fit. Instead the cuts $-0.3 < \Delta E < 0.15$GeV and $5.26 < M_{bc} < 5.29$GeV are performed for a suitable fit window. The asymmetric ΔE cut is due to asymmetries in this variable from photon energy miscalibration and final state radiation.

5.3 Continuum Suppression

As discussed in section 2.6.1, continuum background appears at a rate of $3:1$ compared to a $\Upsilon(4S)$ production at the chosen beam energy and around the beam energy resolution at SuperKEKB. In order to reject the background from continuum events the difference of their event shapes to the shape of signal events can be used. The mass of the $\Upsilon(4S)$ is just enough to produce two B mesons. Thus, in the center of mass frame, the distribution of the B decays is almost spherical. For the lighter continuum events ($u\bar{u}$, $d\bar{d}$, $c\bar{c}$, $s\bar{s}$), the excess energy results in high momenta of the quark and anti-quark in the center of mass frame. Thus, continuum events have a jet-like structure.

This difference can be exploited by a set of variables. One of them is the thrust of a set of particles. Is is given by

$$T = \frac{\sum_i |\vec{n}\vec{p_i}|}{\sum_i |\vec{p_i}|}, \tag{5.4}$$

and projects information about the event shape. $\vec{p_i}$ denotes the momenta of the considered particles, and $\vec{n}$ is a vector, which maximizes the thrust. This variable is 1 if the event is perfectly jet like. Then, all particle momenta are aligned with the axis $\vec{n}$. $\vec{n}$ is chosen so that the thrust is maximized. A spherically distributed decay has no preferred orientation $\vec{n}$, which leads to small values of T. [28]

For an efficient continuum suppression a set of variables associated with the event topology, flavor-tagger information, vertex separation and uncertainty information, and kinematic-fit quality information have been used. These variables are nonlinearly combined by a binary boosted decision-tree classifier into one composed continuum suppression variable (CSV). The boosted decision tree has been trained on a data set of correctly reconstructed signal events and continuum events. Using different combinations of input variables and training samples, different CSVs can be produced. Their performance is evaluated by receiver operating characteristic (ROC) curves, which show the ability of a certain variable to reject continuum background at a given signal efficiency. The variables are tested on a set of 2.5×10^5 signal and 2.5×10^5 continuum events. The resulting ROC curves are shown in figure 5.1. [41]

The best performing variable is as expected the one which has been specifically trained on the signal events of $B^+ \to K^*(892)^+[K^0_S\pi^+]\pi^0$. The most important discrimination variable can be evaluated by looking at the weights used by the resulting CSV. As expected this was an event shape variable here, which returns the cosine of the thrust axis of the reconstructed B meson and the Rest Of the Event (ROE), which contains all particle candidates of the event that are not part of the considered B meson. The discrimination power of the chosen combined CSV is displayed in the following figure.

Now, the selected CSV will be optimized simultaneously with the "pionID". This variable is the probability of a found particle to be a pion in relation to the probability of being an other final state particle. Considering that next to the final state pions in the decay, the K^0_S is reconstructed from the decay into $\pi^+\pi^-$, the pion identification is of high importance for the signal reconstruction. After the loose cuts of the reconstruction, the cut on this variable optimizes the selection. Together with the CSV, both variables have been optimized on the generic MC data set after the already discussed cuts. This lead to the cuts $pionID > 0.12$ and CSV > 0.92.

5.3.1 Momentum Cuts

The decay $B^+ \to K^*(892)^+[K^0_S\pi^+]\pi^0$ is initially only a two-body decay into a pseudoscalar meson (π^0) and a vector meson ($K^*(892)^+$). Hence, the decay products decay back-to-back in the B meson system. The momenta of the two decay products in this system have
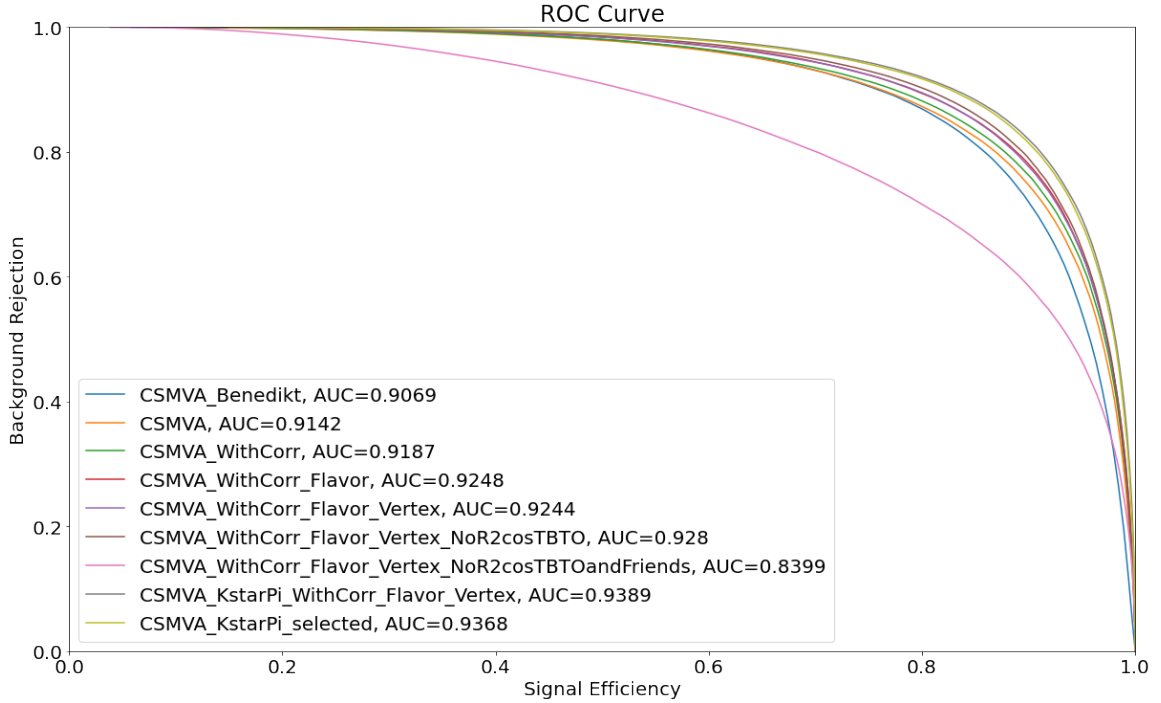
Figure 5.1: *ROC curves for the different CSVs and their respective area under the curve (AUC) values.*

to have the same absolute value due to momentum conservation. Therefore, the π^0 and $K^*(892)^+$ are expected to have a fixed momentum in the B meson rest frame, which is only broadened by resolution effects in the detector. Those variables thus provide excellent discrimination against background. The FOM optimized cut range on the π^0 momentum in the B rest frame has been determined as $2.5 < p_{Brestframe}(\pi^0) < 2.59\text{GeV}$. For the $K^*(892)^+$ the best cuts have been found to be $2.49 < p_{Brestframe}(K^*(892)^+) < 2.59\text{GeV}$. The distributions of signal and background MC events in these variables after the described cuts above are shown in figure 5.3.

The respective momenta of the two final state particles K_S^0 and π^+ coming from the K^{*+} in the B meson rest frame follow a broad momentum distribution. Hence, they have less discriminating power. However, their momenta can be constrained to physically allowed regions. This, combined with the cuts on the π^0 and K^{*+} momentum in the B restframe, can especially reject $B\bar{B}$ background, which may have similar or almost similar final states but different decay topologies. The upper bounds on the momenta in B meson restframe have been constructed using conservation arguments. In the B rest frame, the $K^*(892)^+$ initially carries the energy corresponding to the half of the B mass. After the decay of the
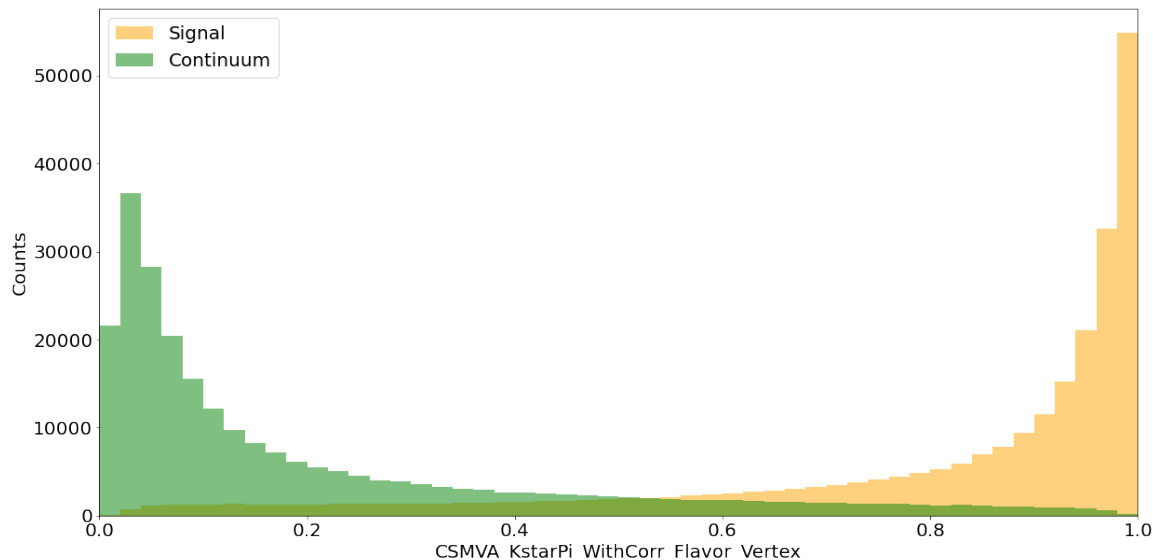
Figure 5.2: *Discrimination power of the chosen CSV between signal and continuum events.*
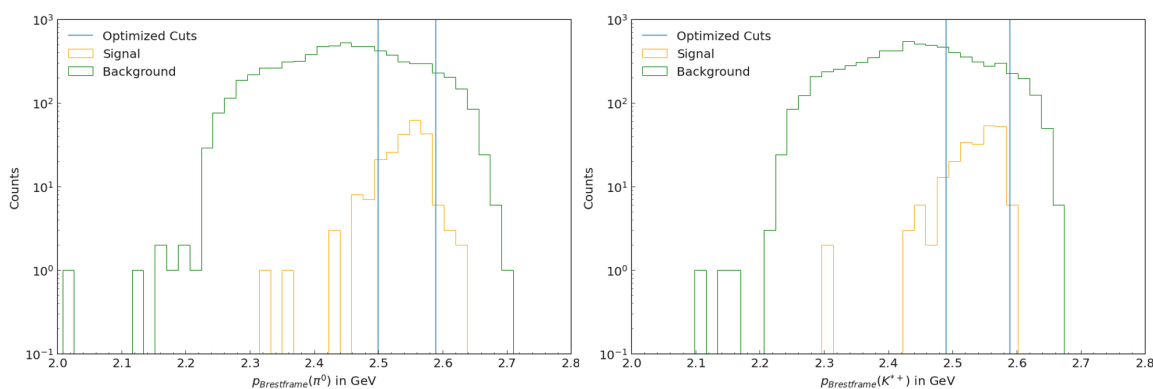
Figure 5.3: *Distribution of signal and background MC events in the variables $p_{Brestframe}(\pi^0)$ (left) and $p_{Brestframe}(K^{*+})$ (right) on a logarithmic scale. The respective FOM optimized cuts are shown by the vertical blue lines.*

$K^*(892)^+$, the K_S^0 and π^+ each carry a maximal energy of the $K^*(892)^+$ energy minus the energy corresponding to the mass of the respective other particle. This maximal value can only be exceeded by signal events due to resolution effects. In order to catch all signal events, a resolution correction factor has been added to the upper bound. This value has been determined from the distributions of the final state particles of signal events in the B rest frame momentum variable as $\delta E_{resolution} = 0.05\text{GeV}$. This leads to the bound calculation in the energy of

$$Bound_{K_S^0/\pi^+} = \frac{m_{B^+}c^2}{2} - m_{\pi^+/K_S^0} + \delta E_{resolution}. \qquad (5.5)$$

The resulting cuts are $p_{Brestframe}(K_S^0) < 2.55\text{GeV}$ and $p_{Brestframe}(\pi^+) < 2.19\text{GeV}$.

Applying the above cuts to the simulated data results in a rejection of 81% of the background and a rejection of 13.8% of the signal events. Instead of using these momentum cuts one can also model the leading individual $B\bar{B}$ background decays. Using the MC truth information of the simulated data, the individual contributions of different $B\bar{B}$ backgrounds can be evaluated. By extracting the shapes of these decay modes in the fitting variables ΔE and M_{bc}, they can then be introduced into the fit. However, this method has not lead to an improved fit quality since the shapes of the background components are too similar to the signal shape in the fit variables. Analyzing the $B\bar{B}$ background after the momentum cuts also shows the suppression power of these cuts. Still, with more statistics it might become advantageous at some point to fit the $B\bar{B}$ background instead of cutting it out.

5.4 Fitting

5.4.1 Branching Ratio

The remaining events after the described selection and cuts will now be fitted. A two dimensional unbinned maximum likelihood fit is performed in the variables ΔE and M_{bc}. Three types of contributions still contribute to the selected sample. The signal, $B\bar{B}$ background and continuum background. Each of these contributions is first considered individually and a probability density function (PDF) model is fit to their shapes. The used shape types are shown in table 5.1.

Decay	Component	ΔE Model	M_{bc} Model
$B^+ \to K^*(892)^+[K_S^0\pi^+]\pi^0$	Signal	Gaussian + Crystal Ball	Gaussian + Crystal Ball
	$B\bar{B}$	2D Kernel PDF	
	Continuum	Gaussian	Argus

Table 5.1: *Fit models for the individual components in the two fit variables ΔE and M_{bc}.*

The used models have been determined empirically. In this process the aim was to find the most basic model which produces a χ^2 close to the degrees of freedom in the respective model. Since the $B\bar{B}$ background follows no analytic shape, it has been modeled by a kernel PDF, which produces a shape of adjustable "smoothness" and matches the events. The "smoothness" factor has also been chosen with regards to the χ^2 value. The signal

shape has been determined from signal only MC with the identical cuts. For the final fit, all shapes have been fixed letting only the respective yields float. The resulting fit is shown in figure 5.4.
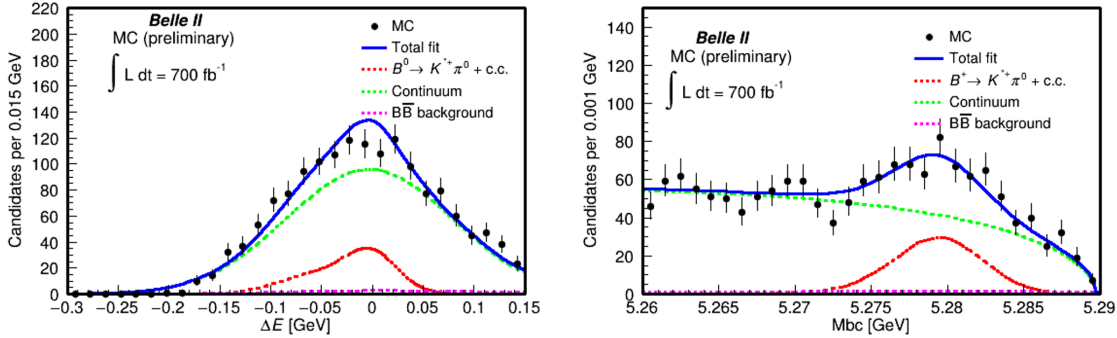
Figure 5.4: *Fit of the event sample in ΔE and M_{bc} with the contributions signal, continuum background and $B\bar{B}$ background.*

The fitted yields of the contributions from the fit compared to the true values in the simulated data are shown in table 5.2.

Component	Fit value	MC truth
Signal	222 ± 26	194
$B\bar{B}$	39 ± 82	266
Continuum	1266 ± 89	1067
Total	1527	1527

Table 5.2: *Fit models for the individual components in the two fit variables ΔE and M_{bc}.*

The results show that the fit successfully combines the different components to form the overall event shapes. The signal, including the desired decay and its charged conjugated decay, can be estimated with a deviation of about 1σ, which is acceptable. However, the fit fails to assign the correct yields to the $B\bar{B}$ and continuum background. Most $B\bar{B}$ events are fit as continuum events. This occurs, since there is no discriminating difference between the shapes of the two components. The respective $B\bar{B}$ and continuum background shapes in ΔE (figure 5.5) and M_{bc} (figure 5.6) are displayed below. It can be senn that in both cases, there are no features in the shapes which enable the differentiation between the shapes.

This could potentially be solved by modeling the $B\bar{B}$ events in more detail. The problem here is that the kernel PDF would cover statistical insignificant shapes then and could
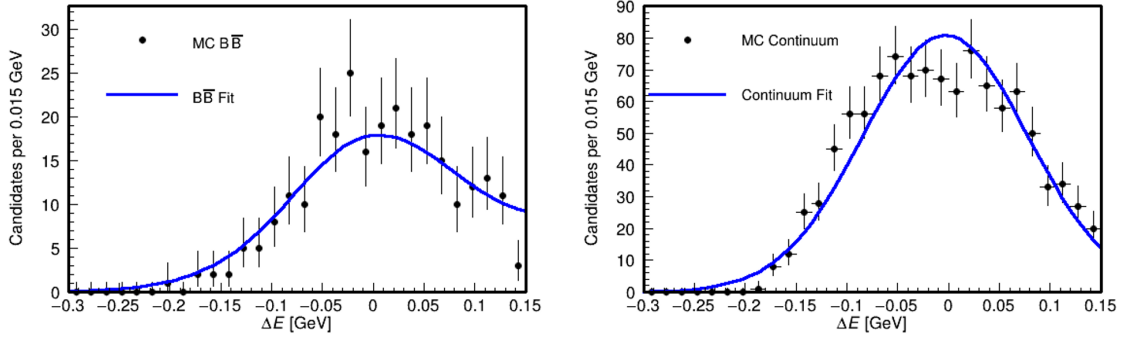
Figure 5.5: *Fit of the $B\bar{B}$ (left) and continuum (right) background MC events in ΔE using the respective shapes from table 5.1.*
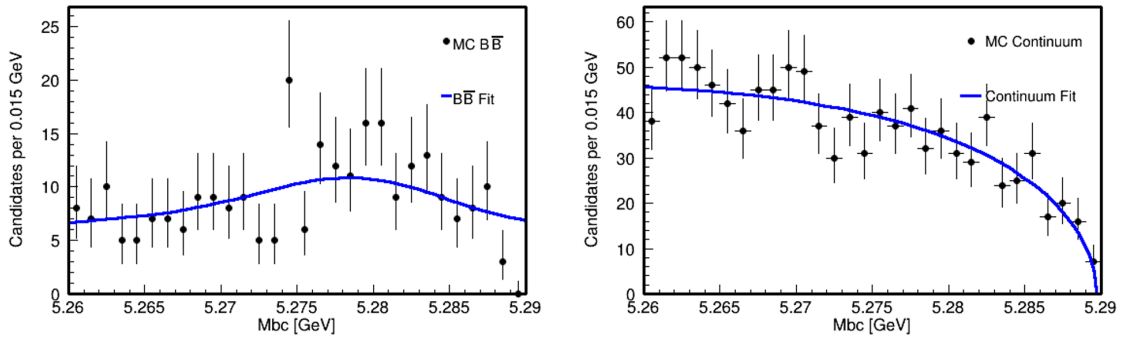
Figure 5.6: *Fit of the $B\bar{B}$ (left) and continuum (right) background MC events in M_{bc} using the respective shapes from table 5.1.*

not be used for the real data. Without using the cuts on the final state particle momenta in the B rest frame, more $B\bar{B}$ are left, which makes the discrimination easier. On the other hand, the statistical significance on the signal is decreased without these cuts. In addition, with more data the differences in the shapes will get more significant, which can help the discrimination.

5.4.2 Direct CP Asymmetry

The fit on the direct CP asymmetry is performed by splitting up the data into positively charged and negatively charged events. The same fixed models for the different contributions are used while the total event number is fixed. Then both event groups can be simultaneously fit after introducing the asymmetry as a free parameter. The results from the fit are displayed in table 5.3.

	Fit value	MC truth
$A_{CP}(B^+ \to K^*(892)^+[K_S^0\pi^+]\pi^0)$	-0.049 ± 0.109	-0.021

Table 5.3:

The first result on the direct CP asymmetry has the same order of magnitude as the MC truth value. Still, the error exceeds the central value by a factor of more than two. In addition, systematic uncertainties are not included in this error value. This result only shows, that a working A_{CP} fit is in place. In order to achieve more significant results, the analysis has to be improved further and the available data sample has to increase.

5.5 Summary

In the current state of the analysis on the decay $B^+ \to K^*(892)^+[K_S^0\pi^+]\pi^0$ the event reconstruction and signal optimization methods allow for a working 2D fit of the events in ΔE and M_{bc}. This fit converges but fails to differentiate between $B\bar{B}$ and continuum background. In addition a functioning A_{CP} fit is in place, which still has large errors compared to the desired result. This result will likely improve with a higher data sample.

As a next step a candidate selection has to introduced to the selection. At the current state, multiple event candidates coming from a single event can pass the selection. Thus, a mechanism choosing one candidate has to be installed. In addition, the systematic uncertainties of this analysis have to be investigated in order to determine the quality of the fit results. Improving the $B\bar{B}$ modeling can also potentially improve the results. If a enhanced $B\bar{B}$ modeling is in place, the momentum cuts are definitely disfavored.

6 Conclusion and Outlook

Since the beginning of data taking in 2019, the Belle II experiment has accumulated about 90fb^{-1} of integrated luminosity until March 2021 [42]. With a steady increase in the instantaneous luminosity aiming for a peak value of $\mathcal{L} = 6 \times 10^{35}\text{cm}^{-2}\,\text{s}^{-1}$, the new Belle II detector with its refined analysis tools will lead the way to the most precise flavor physics measurements in the world and potentially the discovery of NP.

At the current state, the measurements on the $B \to K\pi$ decays show some tensions within the SM. Most notably, the asymmetries $A_{CP}(K^+\pi^0)$ and $A_{CP}(K^+\pi^-)$ show a difference of $\Delta A_{CP} = (0.114 \pm 0.014)$ [13] even though they differ only by a spectator quark. This is known as the $K\pi$-puzzle. In fact, the leading amplitudes of the decay diagrams, the color allowed tree diagram (T') and the electroweak and gluonic penguin diagrams (P', P'_{EW}), fail to explain the measurements. With the introduction of the color suppressed tree amplitude (C') at a fixed magnitude to $\frac{1}{3}$ of the strength of T' and with a free strong phase, the $K\pi$-puzzle can be explained within the SM. This implies that the $K\pi$-puzzle could be solved solely by QCD effects. Also the theory can be fit to the complete set of measurements with a quality of $\frac{\chi^2}{d.o.f.} = 5.6/4$. Introducing an additional constraint from the BR measurement on $B^+ \to \pi^+\pi^0$ helps to constrain the modulus of T' but creates further tensions to the model resulting in an overall fit quality of $\frac{\chi^2}{d.o.f.} = 8.9/5$ with a fixed C' magnitude and $\frac{\chi^2}{d.o.f.} = 7.7/4$ with this strength as a free parameter. Throughout the analysis $B^0 \to K^0\pi^0$ has been identified as a key measurement for the system to potentially resolve the remaining tensions.

Such a detailed analysis is not possible for the $B \to K^*\pi$ system due to a lack of precision in the measurements. However, a fit including all leading amplitudes and the color suppressed decay amplitude with a free modulus could be performed on the data with the quality $\frac{\chi^2}{d.o.f.} = 14.1/2$. This shows the large remaining discrepancies in the measurements. In this case, especially the measurement $A_{CP}(K^{*0}\pi^0)$ deviated from the most likely parameter values. More precise measurements from Belle II will enable a more conclusive analysis.

For the Belle II analysis on the decay channel $B^+ \to K^*(892)^+[K^0_S\pi^+]\pi^0$ the basic event reconstruction and selections are in place. A 2D fit in ΔE and M_{bc} has been worked out in this thesis, which identifies signal events but fails to distinguish $B\bar{B}$ and continuum background. In addition, a working fit on the direct CP asymmetry is installed, which

produces reasonable results, within the error range. Unfortunately the size of the errors at this point is far from competitive to the latest measurements. In addition, before a reasonable result can be extracted from these analysis tools, a best candidate selection has to be introduced and the analysis has to be unblinded in order to determine the systematic uncertainties. This includes among other things errors on the tracking and reconstruction efficiency, the background and signal modeling and potential instrumental asymmetries from the detector, based on suitable control decay channels. Next to the incomplete analysis, the presently accumulated data sample of Belle II is too small for an improvement of especially the $B \to K^*\pi$ data. As more data is collected, the analysis will be enhanced and completed. Large data amounts may change the optimal cuts due to improved $B\bar{B}$ modeling. A complete analysis will eventually yield the most precise measurements on $B^+ \to K^*(892)^+[K_S^0\pi^+]\pi^0$.

7 Appendix

Outline of Derivation for $I_{K\pi}$

This derivation follows Gronau and Rosner [31]. Here, the gluonic penguin amplitude P' is considered as a single decay contribution with a strong and a weak phase. This coincides with the considerations of this thesis regarding the suppression of P'_{uc}. The weak phase of P' is then equal to the weak phases of P'_{EW} and P'^{C}_{EW}. Also, T' and C' have the same weak phase. Thus, no direct CP asymmetry comes from the interference between different penguin amplitudes or between the tree amplitudes. Considering the numerator of the asymmetries, given as

$$\Delta(K^+\pi^0) = \Gamma(B^- \to K^-\bar{\pi^0}) - \Gamma(B^+ \to K^+\pi^0) \tag{7.1}$$

for the decay $B^+ \to K^+\pi^0$ the contributions to the individual asymmetries can be found. The interaction term of two amplitudes is abbreviated by e.g. $\vec{P'}\vec{T'}$ for the interaction of P' and T'. Now, the numerators of the asymmetries are can be calculated from equations 4.2-4.5 as

$$\Delta(K^0\pi^+) = 0, \tag{7.2}$$

$$\Delta(K^+\pi^0) = -\vec{P'}\vec{T'} - \vec{P'}\vec{C'} + (\vec{P'}_{EW} + \frac{2}{3}\vec{P'}^{C}_{EW})(\vec{T'} + \vec{C'}), \tag{7.3}$$

$$\Delta(K^+\pi^-) = -2\vec{P'}\vec{T'} + \frac{4}{3}\vec{P'}^{C}_{EW}\vec{T'}, \tag{7.4}$$

$$\Delta(K^0\pi^0) = \vec{P'}\vec{C'} + \vec{P'}_{EW}\vec{C'} + \frac{1}{3}\vec{P'}^{C}_{EW}\vec{C'}. \tag{7.5}$$

The annihilation amplitude A' is still neglected here. Now, a sum relation can be formed, which is

$$\Delta(K^0\pi^+) + \Delta(K^+\pi^-) \approx 2\Delta(K^+\pi^0) + 2\Delta(K^0\pi^0). \tag{7.6}$$

This equation can be solved as

$$(\vec{P'}_{EW} + \vec{P'}^{C}_{EW})(\vec{T'} + \vec{C'}) + (\vec{P'}_{EW}\vec{C'} - \vec{P'}^{C}_{EW}\vec{T'}) \approx 0. \tag{7.7}$$

It can be seen that all terms including the leading order P' cancel out. The terms $(\vec{P}'_{EW} + \vec{P}'^{C}_{EW})$ and $(\vec{T}' + \vec{C}')$ have approximately the same strong phase [43]. Thus, the term $(\vec{P}'_{EW} + \vec{P}'^{C}_{EW})(\vec{T}' + \vec{C}')$ does not contribute to the direct CP asymmetry in this approximation. The second term vanishes when using equation 4.11 and the analogue approximation for the respective color suppressed counterparts [26]. They can be rearranged to

$$\vec{P}'_{EW}\vec{C}' \approx \vec{P}'^{C}_{EW}\vec{T}', \tag{7.8}$$

which justifies equation 7.6. In order to apply the rule on the actual measurements, the actual BR measurements have to be considered, which ultimately leads to equation 4.10.

List of Figures

List of Tables

Abbreviations

ARICH Aerogel Ring-Imaging CHerenkov Detector

AUC area under the curve

Belle High Energy Physics Experiment and corresponding Detector

BR branching ratio

CDC Central Drift Chamber

CERN Conseil Européen pour la Recherche Nucléaire

CKM Cabibbo-Kobayashi-Maskawa

CSV continuum suppression variable

DEPFET DEpleted P-channel Field Effect Transistor

ECL Electromagnetic Calorimeter

FOM Figure of Merit

GM Gated Mode

HER High Energy Ring

IP Interaction Point

KEK High Energy Physics Research Centre

KEKB KEK B factory

KLM K_L and μ detector

LER Low Energy Ring

LHC Large Hadron Collider

MC Monte Carlo

MPI Max-Planck-Institut

NP New Physics

PDF probability density function

PDG Particle Data Group

PXD Pixel Vertex Detector

ROC receiver operating characteristic

ROE Rest Of the Event

RPC resistive plate chamber

SM Standard Model

SuperKEKB Super KEK B factory

SVD Silicon Vertex Detector

TOP Time of Propagation detector

VXD Vertex detector

Bibliography

[1] A D Sakharov. "VIOLATION OF CP INVARIANCE, C ASYMMETRY, AND BARYON ASYMMETRY OF THE UNIVERSE." In: *JETP Lett. (USSR)(Engl. Transl.), 5: 24-7(Jan. 1, 1967).* (Jan. 1967). URL: https://www.osti.gov/biblio/4449128.

[2] Makoto Kobayashi and Toshihide Maskawa. "CP-Violation in the Renormalizable Theory of Weak Interaction". In: *Progress of Theoretical Physics* 49.2 (Feb. 1973), pp. 652–657. ISSN: 0033-068X. DOI: 10.1143/PTP.49.652. eprint: https://academic.oup.com/ptp/article-pdf/49/2/652/5257692/49-2-652.pdf. URL: https://doi.org/10.1143/PTP.49.652.

[3] K. Abe et al. "Observation of LargeCPViolation in the Neutral B Meson System". In: *Physical Review Letters* 87.9 (Aug. 2001). ISSN: 1079-7114. DOI: 10.1103/physrevlett.87.091802. URL: http://dx.doi.org/10.1103/PhysRevLett.87.091802.

[4] B. Aubert et al. "Observation ofCPViolation in the B0 Meson System". In: *Physical Review Letters* 87.9 (Aug. 2001). ISSN: 1079-7114. DOI: 10.1103/physrevlett.87.091801. URL: http://dx.doi.org/10.1103/PhysRevLett.87.091801.

[5] *Standard Model.* URL: https://en.wikipedia.org/wiki/Standard_Model. (accessed: 13.02.2021).

[6] *The Higgs boson.* URL: https://home.cern/science/physics/higgs-boson. (accessed: 28.01.2019).

[7] David Griffiths. *Introduction to Elementary Particles.* WILEY-VCH Verlag GmbH & Co. KGaA, 2008.

[8] E. Noether. "Invariante Variationsprobleme". ger. In: *Nachrichten von der Gesellschaft der Wissenschaften zu Göttingen, Mathematisch-Physikalische Klasse* 1918 (1918), pp. 235–257. URL: http://eudml.org/doc/59024.

[9] Felix Benjamin Müller. "Characterization and Optimization of the Prototypes DEPFET Modules for the Belle II Pixel Vertex Detector". PhD thesis. Fakultät für Physik der Ludwig–Maximilians- Universität München, 2017. URL: http://www.mpp.mpg.de/~cmk/Belle/Thesis_Mueller_Felix.pdf.

[10] Klaus Hentschel Friedel Weinert Daniel Greenberger. *Compendium of Quantum Physics.* Springer, 2009. Chap. CPT Theorem by Klaus Kiefer.

[11] Markus Reif. "Optimization of the new Pixel Vertex Detectorfor Physics Running in the Belle II Experiment". masterthesis. Fakultät für Physik der Ludwig–Maximilians-Universität München, 2019.

[12] J. H. Christenson et al. "Evidence for the 2π Decay of the K_2^0 Meson". In: *Phys. Rev. Lett.* 13 (4 July 1964), pp. 138–140. DOI: `10.1103/PhysRevLett.13.138`. URL: `https://link.aps.org/doi/10.1103/PhysRevLett.13.138`.

[13] Particle Data Group et al. "Review of Particle Physics". In: *Progress of Theoretical and Experimental Physics* 2020.8 (Aug. 2020). 083C01. ISSN: 2050-3911. DOI: `10.1093/ptep/ptaa104`. eprint: `https://academic.oup.com/ptep/article-pdf/2020/8/083C01/34673722/ptaa104.pdf`. URL: `https://doi.org/10.1093/ptep/ptaa104`.

[14] M. Pimenta A. De Angelis. *Introduction to Particle and Astroparticle Physics*. Springer, 2018.

[15] Thomas Kuhr. *Flavor Physics at the Tevatron*. Springer, 2013.

[16] Nicola Cabibbo. "Unitary Symmetry and Leptonic Decays". In: *Phys. Rev. Lett.* 10 (1963), pp. 531–533. DOI: `10.1103/PhysRevLett.10.531`.

[17] Lincoln Wolfenstein. "Parametrization of the Kobayashi-Maskawa Matrix". In: *Phys. Rev. Lett.* 51 (1983), p. 1945. DOI: `10.1103/PhysRevLett.51.1945`.

[18] *CKM Fitter*. URL: `http://ckmfitter.in2p3.fr/www/results/plots_summer19/ckm_res_summer19.html`. (accessed: 19.02.2021).

[19] *Y(4S)-Particle Data Group*. URL: `https://pdg.lbl.gov/2014/listings/rpp2014-list-upsilon-4S.pdf`. (accessed: 19.02.2021).

[20] *First particles circulate in SuperKEKB accelerator*. URL: `https://phys.org/news/2016-04-particles-circulate-superkekb.html`. (accessed: 02.03.2021).

[21] *Present design of SuperKEKB*. URL: `https://indico.cern.ch/event/47961/contributions/1989731/attachments/956118/1356921/SuperKEKB.pdf`. (accessed: 10.03.2021).

[22] Kazunori Akai, Kazuro Furukawa, and Haruyo Koiso. "SuperKEKB collider". In: *Nuclear Instruments and Methods in Physics Research Section A: Accelerators, Spectrometers, Detectors and Associated Equipment* 907 (Nov. 2018), pp. 188–199. ISSN: 0168-9002. DOI: `10.1016/j.nima.2018.08.017`. URL: `http://dx.doi.org/10.1016/j.nima.2018.08.017`.

[23] Boqun Wang. *Searches for New Physics at the Belle II Experiment*. 2015. arXiv: `1511.00373 [hep-ex]`.

[24] Sara Pohl and Christian Kiesling. "Track Reconstruction at the First Level Trigger of the Belle II Experiment". Presented on 11 04 2018. PhD thesis. Munich: Munich, Ludwig-Maximilians-Universität, 2018.

[25] W. Altmannshofer et al. "The Belle II Physics Book". In: *PTEP* 2019.12 (2019). Ed. by E. Kou and P. Urquijo. [Erratum: PTEP 2020, 029201 (2020)], p. 123C01. DOI: 10.1093/ptep/ptz106. arXiv: 1808.10567 [hep-ex].

[26] Nicolas Boisvert Beaudry et al. *The $B \to \pi K$ Puzzle Revisited*. 2018. arXiv: 1709.07142 [hep-ph].

[27] *Electrons and Positrons Collide for the first time in the SuperKEKB Accelerator*. URL: https://www.kek.jp/en/newsroom/2018/04/26/0700/. (accessed: 18.01.2019).

[28] Kolja Andreas Prothmann. "Measurement of Branching Ratiosand CP Asymmetries for the decays $B^0 \to \pi^+\pi^-$, $B^0 \to K^+\pi^-$, $B^0 \to K^+K^-$". PhD thesis. Fakultät für Physik der Ludwig–Maximilians- Universität München, 2012.

[29] Hai-Yang Cheng, Cheng-Wei Chiang, and An-Li Kuo. "Updating $B \to PP, VP$ decays in the framework of flavor symmetry". In: *Physical Review D* 91.1 (Jan. 2015). ISSN: 1550-2368. DOI: 10.1103/physrevd.91.014011. URL: http://dx.doi.org/10.1103/PhysRevD.91.014011.

[30] Robert Fleischer, Ruben Jaarsma, and K. Keri Vos. "Towards new frontiers with $B \to \pi K$ decays". In: *Physics Letters B* 785 (Oct. 2018), pp. 525–529. ISSN: 0370-2693. DOI: 10.1016/j.physletb.2018.09.015. URL: http://dx.doi.org/10.1016/j.physletb.2018.09.015.

[31] Michael Gronau and Jonathan L. Rosner. "Combining CP asymmetries in $B \to K\pi$ decays". In: *Physical Review D* 59.11 (Apr. 1999). ISSN: 1089-4918. DOI: 10.1103/physrevd.59.113002. URL: http://dx.doi.org/10.1103/PhysRevD.59.113002.

[32] Michael Gronau. "Electroweak penguin amplitudes and constraints on γ in charmless $B \to VP$ decays". In: *Physical Review D* 62.1 (June 2000). ISSN: 1089-4918. DOI: 10.1103/physrevd.62.014031. URL: http://dx.doi.org/10.1103/PhysRevD.62.014031.

[33] *Statistical Methods in Particle Physics*. URL: https://www.physi.uni-heidelberg.de/~reygers/lectures/2017/smipp/stat_methods_ss2017_05_parameter_estimation.pdf. (accessed: 09.02.2021).

[34] E.Lohrmann V. Blobel. *Statistische und numerischeMethoden der Datenanalyse*. Teubner Studienbücher, 1998.

[35] Will Parker. "Direct CP violation in the decay B+ to K+ pi0 at LHCb. Direct CP violation in the decay B+ to K+ pi0 at LHCb". In: (Dec. 2020). URL: https://cds.cern.ch/record/2746303.

[36] Martin Beneke. private communication.

[37] Robert Fleischer et al. "Exploring $B \to \pi\pi, \pi K$ Decays at the High-Precision Frontier". In: *The European Physical Journal C* 78.11 (Nov. 2018). ISSN: 1434-6052. DOI: 10.1140/epjc/s10052-018-6397-5. URL: http://dx.doi.org/10.1140/epjc/s10052-018-6397-5.

[38] Belle II Collaboration et al. *Measurements of branching fractions and CP-violating charge asymmetries in charmless B decays reconstructed in 2019–2020 Belle II data.* 2020. arXiv: 2009.09452 [hep-ex].

[39] T. Keck et al. "The Full Event Interpretation". In: *Computing and Software for Big Science* 3.1 (Feb. 2019). ISSN: 2510-2044. DOI: 10.1007/s41781-019-0021-8. URL: http://dx.doi.org/10.1007/s41781-019-0021-8.

[40] Giovanni Punzi. *Sensitivity of searches for new signals and its optimization.* 2003. arXiv: 0308063 [physics].

[41] Belle II Collaboration et al. *Charmless B decay reconstruction in 2019 Belle II data.* 2020. arXiv: 2005.13559 [hep-ex].

[42] *Belle II Luminosity.* URL: https://confluence.desy.de/display/BI/Belle+II+Luminosity. (accessed: 28.02.2021).

[43] Michael Gronau, Dan Pirjol, and Tung-Mow Yan. "Model-independent electroweak penguins in B decays to two pseudoscalars". In: *Phys. Rev. D.* 60 (1999). DOI: 10.1103/PhysRevD.60.034021. URL: https://link.aps.org/doi/10.1103/PhysRevD.60.034021.

Danksagung

Erklärung

Hiermit erkläre ich, die vorliegende Arbeit selbständig verfasst zu haben und keine anderen als die in der Arbeit angegebenen Quellen und Hilfsmittel benutzt zu haben.

München, den 14. 03. 2021